Modal and nonmodal stability analysis of turbulent stratified channel flows

Donato Variale,[1,2,*] Enza Parente,[1,2] Jean Christophe Robinet,[2] and Stefania Cherubini[1]
[1]*Dipartimento di Meccanica, Matematica e Management, Politecnico di Bari, Via Re David 200, 70125 Bari, Italy*
[2]*Laboratoire DynFluid, Arts et Métiers ParisTech, 151 Bd de l'Hopital, 75013 Paris, France*

(Received 17 April 2023; accepted 22 November 2023; published 29 January 2024)

Unstable or optimally growing perturbations of turbulent flows are often representative of the energy-containing coherent structures populating the flow, as for streaks in a turbulent channel. Within this framework, this work aims at studying the modal and nonmodal stability of stably stratified turbulent channel flow, assessing the influence of stratification while changing the friction Richardson number, Ri_τ, at fixed friction Reynolds number, Re_τ. When increasing the stratification of the flow, the energy gain for streamwise-independent perturbations at the outer peak increases by two orders of magnitude, and the spanwise wavenumber for which the energy gain peaks reaches values comparable to those reported in the direct numerical simulations of Garcia-Villalba and Del Alamo. At the same time, the value of the optimal gain for the inner peak slightly changes, corroborating the observations made through direct numerical simulation (DNS) about the fact that the wall cycle is not altered by the presence of stratification. Moreover, for nonzero values of the streamwise and spanwise wavenumbers, α and β, the energy gain curve has two peaks, one for shorter target times and $\alpha > \beta$, leading to a center-channel temperature peak, and another occurring for $\alpha < \beta$ at larger target times. In the former case, energy production is mostly linked to velocity production, whereas, in the latter case, the strongest term is that of temperature production, indicating that this mechanism is driven by the increase of the potential energy rather than the kinetic one, and it is intimately linked to the presence of stratification. For strong stratification, the optimal energy gain considerably extends towards higher values of α, leading to energy amplifications reaching three orders of magnitudes for values of α up to 2. The associated optimal perturbations are characterized by temperature patches at the center channel, phase lagged by $\pi/2$ with the wall-normal velocity, similarly to gravity waves recovered in the DNS for sufficiently large stratification. However, for large values of β, we observe an increasing asymmetry in the optimal perturbations, probably due to the shielding effect of the core of the channel, as also observed in the DNS of Garcia-Villalba and Del Alamo.

DOI: 10.1103/PhysRevFluids.9.013904

I. INTRODUCTION

Thermally stratified shear flows are receiving increasing interest as the basis of many meteorological and geophysical applications. In the case of incompressible flows, stratification effects are taken into account in the momentum equation through the addition of buoyancy forces. The latter occur if the flow configuration taken into account is subjected to gravity [1]. In these conditions, a stratified flow can be defined as a flow whose density varies only in the direction in which gravity acts. Thermal stratification is said to be stable (unstable), when the density decreases (increases)

*d.variale@phd.poliba.it

upwards and, consequently, the temperature increases (decreases). The potential energy is greater in unstable than in stable cases; therefore, in the former case, perturbations tend to bring the flow to a (lowest-energy) stable state [2]. An example of the effect of unstable stratification that can be observed in nature are the cloud streets in the atmospheric boundary layer, which consist in organized roll vortices: clouds form in the ascending part of the rolls while on the descending side cloudless areas are recovered [3,4].

A first attempt of a stability study of a thermally stratified shear flow was made by Gage and Reid [5]. They showed that, in the unstable stratification case, there are two types of instability: a thermal mode which leads to steady convection in the form of longitudinal rolls and an inertial mode which is associated to the classic Tollmien-Schlichting mechanism. Then, Asai [6] proved that the switch between these mechanism is linked to the value of the Richardson number, Ri. For $\mathrm{Ri} \approx 10^{-2}-10^{-1}$ the thermal mode is observed, while for lower values of Ri, the inertial one is found. In their work, Jerome *et al.* [7] went further by conducting a nonmodal analysis to study the transient growth of perturbations for unstable stratification in the case of Couette and Poiseuille flow. For small times, it has been observed that the maximum energy gain $G_{\max}$ increases slightly by increasing the Rayleigh number Ra and reducing the Prandtl number Pr. Notably, optimal perturbations produce longitudinal streaks and convective vortices.

On the other hand, stable stratification has been proven to have a stabilizing effect, as in the work of Biau and Bottaro [8]. Among different works, Facchini *et al.* [9] performed a stability analysis of a stably stratified plane Couette flow with a constant density gradient orthogonal to the shear. In this configuration, unstable modes are found for a Reynolds number $\mathrm{Re} = 700$ and a Froude number $\mathrm{Fr} = 1$. Furthermore, the range of unstable Fr increases with Re and instability only occurs for three-dimensional (3D) perturbations in opposition to what Squire's theorem assumes. Recently, Parente *et al.* [10] considered the stably stratified Blasius boundary layer flow in terms of modal and nonmodal stability. Using a modal approach, they found that increasing Ri leads to a stabilization of the flow, whereas with the nonmodal approach they observed that increasing Ri leads to a reduction of the optimal time and the optimal energy gain, and that the latter occurs for nonzero values of the streamwise wavenumber. Moreover, the energy changes from a quadratic dependence on Re to a linear one and the optimal mechanism is due to a combined effect of the Orr mechanism and the lift-up mechanism.

All the works cited so far have one point in common; namely, they all consider the stability of laminar stratified flows, whose instability would lead to a turbulent state [11]. However, when examining the stability of a turbulent flow, the situation becomes more complex. Two main approaches are used in the literature.

The first, the *quasilaminar* approach, consists in using the Navier-Stokes equations linearized around a turbulent velocity field while eliminating the Reynolds stress or including them in a forcing term [12]. In this way, the linear operator remains the same as in the laminar case. An example of this quasilaminar method may be found in the work of McKeon and Sharma [13]. Through singular value decomposition of the resolvent operator of a turbulent pipe flow, they have discovered two types of response modes by varying the frequency of the forcing: a wall-response mode and a critical-response mode characterized by a streamwise wave speed similar to the local mean velocity at the peak of streamwise energy.

The second approach is referred to as *statistically linear* and is based on a triple decomposition [14,15] of the flow variables $\mathbf{q}$, dividing them in a long-time-averaged part $\overline{\mathbf{q}}$ plus a coherent phase-averaged disturbance $\mathbf{q}'$ and the incoherent fluctuation $\mathbf{q}''$ (where $\bar{\cdot}$ is the average operator and $\overline{\mathbf{q}''} = 0$). Then, the Reynolds stress tensor is taken into account by means of models such as the eddy viscosity ν_t. An example of this approach is the work of Pujals *et al.* [16] on the turbulent channel flow that will be discussed later as a reference case.

In the field of unstably stratified flows, some recent works considered the stability of stratified turbulent channel flows. Madhusudanan *et al.* [17] studied the response of the linear Navier-Stokes operator to impulses located in the center of the channel and at the wall in the case of the turbulent stratified channel flow for different values of bulk Richardson number Ri_b. Their reference work

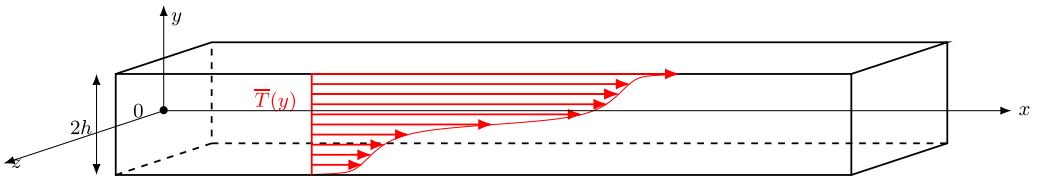

FIG. 1. Scheme of the channel flow with its scales and a representation of the mean temperature $\overline{T}(y)$.

was the direct numerical simulation (DNS) performed by Pirozzoli *et al.* [18] from which they take the mean velocity and temperature fields. They observed that, for a zero streamwise wavenumber, by increasing Ri_b the streamwise-independent structures passed from having one peak intensity at the center of the channel to having two peaks close to the wall. Using the same data set, Cossu [19] investigated the linear stability of the operator, retrieving the critical friction Richardson number for which large-scale uniform streamwise-uniform coherent rolls are formed, that is, $\mathrm{Ri}_{\tau,c} \approx 0.86$ for Re_b ranging from $\approx 10^4$ to $\approx 10^6$.

Despite the recent body of work on these unstable cases, the stability of a stably stratified turbulent channel flow has never been studied in detail, the only exception being a very recent work by Ahmed *et al.* [20], where resolvent analysis is performed and compared to DNS. The authors show that the resolvent is able to predict coherent structures in the flow with much lower computational costs than a direct simulation. However, the asymptotic stability as well as the optimal perturbations allowing the maximum possible energy gain have never been investigated for this flow. To fill this gap, this work aims at studying the modal and nonmodal stability of stably stratified turbulent channel flow by assessing the influence of stratification on the shear increasing the friction Richardson number Ri_τ with a fixed friction Reynolds number Re_τ. To do this, we will use the data set of Garcia-Villalba and del Alamo [21] obtained by direct numerical simulation of a stably stratified turbulent flow. In this work, they studied the influence of stratification noting that near-wall streaks remain unaltered while buoyancy effects are visible in the center of the channel, where for values of $\mathrm{Ri}_\tau = 1920$ laminar patches start to appear.

In the present work, we will consider the stably stratified turbulent channel flow at three different values of Ri_τ, namely 60, 120, and 480. For these three cases we will examine the modal stability of the linear operator, followed by nonmodal analysis to investigate the energy growth at short times. In fact, perturbations of the mean turbulent flow ensuring an optimal growth of the energy may be representative of the energy-containing coherent structures populating the turbulent flow, as for streaks in the turbulent channel flow [22]. Towards this end, a direct-adjoint method will be used, as by Parente *et al.* [10,23].

The paper is organized as follows: In Sec II the problem is described and the model and equations used to perform the modal and the nonmodal analysis are presented, in Sec. III are reported the results compared with the unstratified case, then in Secs. III A–III C are provided the results for cases $\mathrm{Ri}_\tau = 60$, $\mathrm{Ri}_\tau = 120$, and $\mathrm{Ri}_\tau = 480$, respectively. Finally in Sec. IV conclusions and perspectives are shown.

II. PROBLEM FORMULATION

The dynamics of an incompressible, turbulent, stably stratified channel flow, showed in Fig. 1, can be described by the following set of governing equations:

$$\nabla \cdot \mathbf{u} = 0, \tag{1a}$$

$$\rho \frac{\partial \mathbf{u}}{\partial t} + \rho(\mathbf{u} \cdot \nabla)\mathbf{u} = -\nabla p + \nabla \cdot [\mu(\nabla \mathbf{u} + \nabla \mathbf{u}^T)] - \rho g \mathbf{e}_y, \tag{1b}$$

$$\frac{\partial T}{\partial t} + (\mathbf{u} \cdot \nabla)T = \nabla \cdot [\kappa \nabla T], \tag{1c}$$

$$\rho = \rho_0[1 - \alpha(T - T_0)], \tag{1d}$$

where $\mathbf{u} = (u, v, w)^T$ is the instantaneous velocity vector, p is the pressure, ρ is the density, μ is the dynamic viscosity, g is the gravitational acceleration, and $\mathbf{e}_y$ is the unit vector in the wall-normal direction y. Streamwise and spanwise directions are respectively represented by x and z, T is the temperature, κ is the thermal diffusivity, and ρ_0 and T_0 are respectively the density and temperature of Ref. [24]. Equations (1) are the incompressible Navier-Stokes equations, while Eq. (1d) is the Boussinesq relation that links temperature with density.

A. Model and equations

The instantaneous physical quantities describing the system, $\mathbf{q}(\mathbf{x}, t) = (\mathbf{u}, T, p)^T$, can be expanded as the sum of their long-time average, $\overline{\mathbf{q}}(\mathbf{x})$, and an infinitesimal fluctuation $\mathbf{q}'(\mathbf{x}, t)$:

$$\mathbf{q}(\mathbf{x}, t) = \overline{\mathbf{q}}(\mathbf{x}) + \mathbf{q}'(\mathbf{x}, t). \tag{2}$$

This development is injected into Eqs. (1) and the mean is taken. Finally, the equations for the mean flow are written:

$$\nabla \cdot \overline{\mathbf{u}} = 0, \tag{3a}$$

$$\rho(\overline{\mathbf{u}} \cdot \nabla)\overline{\mathbf{u}} = -\nabla \overline{p} + \nabla \cdot [\mu(\boldsymbol{\nabla}\overline{\mathbf{u}} + \boldsymbol{\nabla}\overline{\mathbf{u}}^T) - \rho\overline{\mathbf{u}'\mathbf{u}'}] - \rho g \mathbf{e}_y, \tag{3b}$$

$$(\overline{\mathbf{u}} \cdot \nabla)\overline{T} = \nabla \cdot [\kappa \nabla \overline{T} - \overline{\mathbf{u}'T'}]. \tag{3c}$$

The system of Eqs. (3) is closed by using the Boussinesq hypothesis allowing to approximate the tensors $-\rho\overline{\mathbf{u}'\mathbf{u}'}$ and $-\overline{\mathbf{u}T'}$ through a turbulent eddy viscosity ν_t and a turbulent thermal eddy diffusivity κ_t:

$$-\overline{\mathbf{u}'\mathbf{u}'} = \nu_t(\boldsymbol{\nabla}\overline{\mathbf{u}} + \boldsymbol{\nabla}\overline{\mathbf{u}}^T), \quad -\overline{\mathbf{u}'T'} = \kappa_t \nabla \overline{T}, \tag{4}$$

which, for a channel flow, becomes

$$-\overline{u'v'} = \nu_t \frac{\partial \overline{u}}{\partial y}, \quad -\overline{v'T'} = \kappa_t \frac{\partial \overline{T}}{\partial y}. \tag{5}$$

Equations (3) are then subtracted from Eqs. (1). The resulting system is linearized and scaled with respect to the outer scale variables, namely, the velocity at center of the channel, U_c, the half-channel height h, and the temperature difference between the two walls, ΔT, providing the following set of equations for the perturbation:

$$\nabla \cdot \mathbf{u}' = 0, \tag{6a}$$

$$\frac{\partial \mathbf{u}'}{\partial t} + (\mathbf{u}' \cdot \nabla)\overline{\mathbf{u}} + (\overline{\mathbf{u}} \cdot \nabla)\mathbf{u}' = -\nabla p' + \frac{1}{\mathrm{Re}}[\nabla \overline{\nu}_t \cdot (\boldsymbol{\nabla}\mathbf{u}' + \boldsymbol{\nabla}\mathbf{u}'^T) + \overline{\nu}_T \nabla^2 \mathbf{u}'] + \mathrm{Ri} T' \mathbf{e}_y, \tag{6b}$$

$$\frac{\partial T'}{\partial t} + (\mathbf{u}' \cdot \nabla)\overline{T} + (\overline{\mathbf{u}} \cdot \nabla)T' = \frac{1}{\mathrm{RePr}}(\nabla \overline{\kappa}_t \cdot \nabla T' + \overline{\kappa}_T \nabla^2 T'), \tag{6c}$$

where $\mathrm{Re} = U_c h/\nu$, $\mathrm{Pr} = \nu/\kappa$, and $\mathrm{Ri} = \alpha \Delta T h g/U_c^2$ are the Reynolds, Prandtl, and Richardson numbers, respectively, while $\overline{\nu}_T = (\nu_t + \nu)/\nu$, $\overline{\nu}_t = \nu_t/\nu$, $\overline{\kappa}_T = (\kappa_t + \kappa)/\kappa$, and $\overline{\kappa}_t = \kappa_t/\kappa$. For simplicity we will assume that ν_t and κ_t are not perturbed.

Since we consider a turbulent flow, there is no analytical formulations for the mean velocity and temperature, as well as for the eddy viscosity and thermal eddy diffusivity. In nonstratified channel flows, it has been demonstrated that, evaluating $\overline{\nu_T}$ using the Cess [25] profile, the linearized Navier-Stokes equations augmented with the eddy viscosity correctly predict the length scales of the turbulent coherent structures [13,16,26,27]. Since here we deal with a stratified channel flow, the eddy viscosity and diffusivity wall-normal profiles, as well as the mean velocity and temperature fields, are evaluated on the basis of the data of Garcia-Villalba and Del Alamo [21]. This set of data has been obtained through a DNS performed at fixed $\mathrm{Re}_\tau = 550$ ($\mathrm{Re} = 11390.6$) and for different

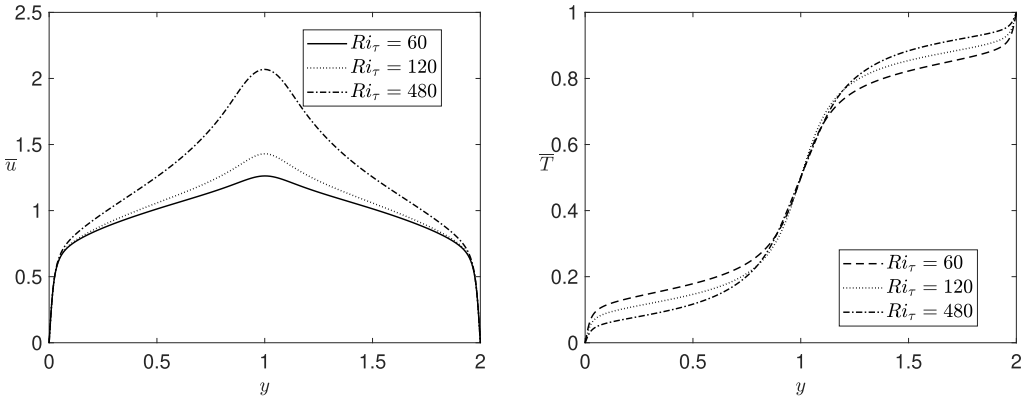

FIG. 2. Streamwise velocity $\overline{u}$ (left) and temperature $\overline{T}$ (right) for $\mathrm{Re}_\tau = 550$ and $\mathrm{Ri}_\tau = 60$, $\mathrm{Ri}_\tau = 120$, and $\mathrm{Ri}_\tau = 480$.

Ri_τ, where $\mathrm{Re}_\tau = u_\tau h/\nu$, $\mathrm{Ri}_\tau = \alpha \Delta T h g/u_\tau^2$, and $u_\tau = \sqrt{\tau_w/\rho}$. In this work, we have used data at $\mathrm{Ri}_\tau = 60$, 120, and 480.

While the mean flow (see Fig. 2) has been simply extracted from the DNS data without further treatment, for ν_t and κ_t we first tried using the model proposed by Eq. (5). However, the resulting profiles were discontinuous and showed strongly oscillating derivatives, leading to numerical instability. Thus, as proposed in Ref. [28], we used a modified Cess formula [25] based on several parameters, reported in Table I, whose value is obtained by least-square fitting of the DNS data. Improving the parameters used in Ref. [28] and adding a further one in order to have a better fitting of the data from the DNS, we use for $\mathrm{Ri}_\tau = 60$ and $\mathrm{Ri}_\tau = 120$

$$\overline{\nu_T} = \left[\frac{1}{2}(1 + a(by + cy^2)^2(d + ey + fy^2)^2(1 - e^{-gy})^2)^{\frac{1}{2}} + \frac{1}{2}\right]\frac{1}{h}, \tag{7}$$

$$\overline{\kappa_T} = \left[\frac{1}{2}(1 + a(by + cy^2)^2(d + ey + fy^2)^2(1 - e^{-gy})^2)^{\frac{1}{2}} + \frac{1}{2}\right]\frac{1}{h\mathrm{Pr}}. \tag{8}$$

The above analytical expressions for $\overline{\nu_T}$ and $\overline{\kappa_T}$ change for $\mathrm{Ri}_\tau = 480$ since in this case the polynomial should tend to zero at the center of the channel, leading to

$$\overline{\nu_T} = \left[\frac{1}{2}(1 + a(by + cy^2)^2(d + ey + fy^2)^2(1 - y^2)(1 - e^{-gy})^2)^{\frac{1}{2}} + \frac{1}{2}\right]\frac{1}{h}, \tag{9}$$

$$\overline{\kappa_T} = \left[\frac{1}{2}(1 + a(by + cy^2)^2(d + ey + fy^2)^2(1 - y^2)(1 - e^{-gy})^2)^{\frac{1}{2}} + \frac{1}{2}\right]\frac{1}{h\mathrm{Pr}}. \tag{10}$$

The new parameters are reported in Table II and the resulting eddy-viscosity and eddy-diffusivity profiles are provided in Fig. 3, showing a very good agreement with the DNS data in Ref. [21], as shown in Appendix C. The relative discrepancy, measured by summing the squares of the difference between the data and the fitted analytical expression, are of order $10^{-6}-10^{-5}$, as reported in Table III.

TABLE I. Values of parameters for $\overline{\nu_T}$ modeling in Eqs. (7) for $\mathrm{Ri}_\tau = 60$, 120, and Eq. (9) for $\mathrm{Ri}_\tau = 480$.

Ri_τ	Ri	a	b	c	d	e	f	g	h
60	0.139878	640	6.139	−3.089	3.651	−7.144	3.571	22.01	1.17
120	0.2797757	610	5.269	−2.644	3.335	−6.607	3.301	22.02	1.08
480	1.11910287	620	4.666	−2.342	3.284	−6.11	3.0571	32.02	0.99

TABLE II. Values of parameters for $\overline{\kappa_T}$ modeling in Eqs. (8) for $\mathrm{Ri}_\tau = 60$, 120, and Eq. (10) for $\mathrm{Ri}_\tau = 480$.

Ri_τ	Ri	a	b	c	d	e	f	g	h
60	0.139878	670	4.84	−2.436	3.219	−6.33	3.152	22	1.0
120	0.2797757	392.5	5.176	−2.601	3.382	−6.706	3.361	22	1.08
480	1.11910287	670	3.755	−1.886	2.986	−5.539	2.776	31.99	1.01

B. Modal stability analysis

For this flow configuration, the assumption of parallel flow can be assumed valid; i.e., the flow has two homogeneous directions x and z. This means that $\nu_t = \nu_t(y)$, $\kappa_t = \kappa_t(y)$, and that

$$\overline{u} = (\overline{u}(y), 0, 0), \quad \overline{T} = \overline{T}(y).$$

The solution for the local stability problem is found in this form:

$$\mathbf{q}'(\mathbf{x}, t) = \hat{\mathbf{q}}(y) e^{i(\alpha x + \beta z - \omega t)} + \text{c.c.}, \tag{11}$$

where α and β are the wavenumbers in the x and z directions, respectively. Using the hypothesis mentioned above and replacing Eq. (11) in Eqs. (6a)–(6c), the following system of equations is obtained,

$$i\alpha\hat{u} + \frac{d\hat{v}}{dy} + i\beta\hat{w} = 0, \tag{12}$$

$$i(\alpha\overline{u} - \omega)\hat{u} + \frac{d\overline{u}}{dy}\hat{v} = -i\alpha\hat{p} + \frac{1}{\mathrm{Re}}\left[\frac{d\overline{\nu}_t}{dy}\frac{d\hat{u}}{dy} + i\alpha\frac{d\overline{\nu}_t}{dy}\hat{v} + \overline{\nu}_T\left(\frac{d^2}{dy^2} - (\alpha^2+\beta^2)\right)\hat{u}\right], \tag{13}$$

$$i(\alpha\overline{u} - \omega)\hat{v} = -i\alpha\frac{d\hat{p}}{dy} + \frac{1}{\mathrm{Re}}\left[2\frac{d\overline{\nu}_t}{dy}\frac{d\hat{v}}{dy} + \overline{\nu}_T\left(\frac{d^2}{dy^2} - (\alpha^2+\beta^2)\right)\hat{v}\right] + \mathrm{Ri}\hat{T}, \tag{14}$$

$$i(\alpha\overline{u} - \omega)\hat{w} = -i\beta\hat{p} + \frac{1}{\mathrm{Re}}\left[\frac{d\overline{\nu}_t}{dy}\frac{d\hat{w}}{dy} + i\beta\frac{d\overline{\nu}_t}{dy}\hat{v} + \overline{\nu}_T\left(\frac{d^2}{dy^2} - (\alpha^2+\beta^2)\right)\hat{w}\right], \tag{15}$$

$$i(\alpha\overline{u} - \omega)\hat{T} + \frac{d\overline{T}}{dy}\hat{v} = \frac{1}{\mathrm{RePr}}\left[\frac{d\overline{\kappa}_t}{dy}\frac{d\hat{T}}{dy} + \overline{\kappa}_T\left(\frac{d^2}{dy^2} - (\alpha^2+\beta^2)\right)\hat{T}\right], \tag{16}$$

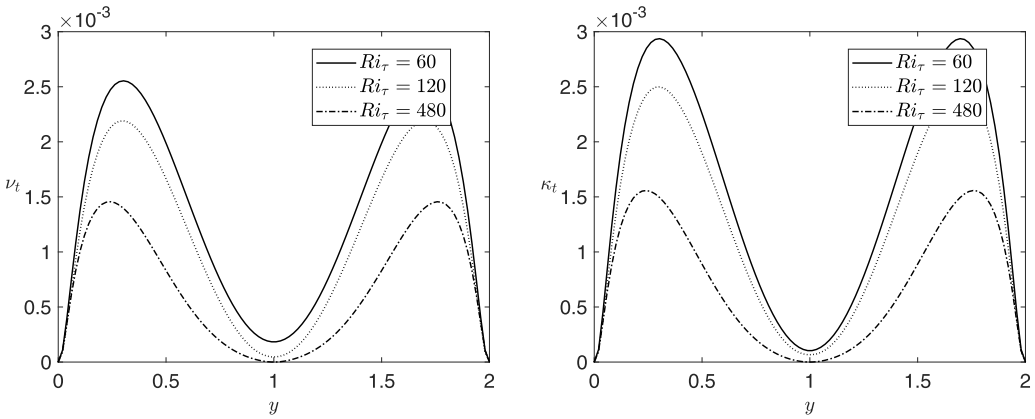

FIG. 3. Eddy viscosity ν_t (left) and thermal eddy diffusivity κ_t (right) for $\mathrm{Re}_\tau = 550$ and $\mathrm{Ri}_\tau = 60$, $\mathrm{Ri}_\tau = 120$, and $\mathrm{Ri}_\tau = 480$.

TABLE III. Values of SSE computed for ν_t and κ_t for $\mathrm{Ri}_\tau = 60$, $\mathrm{Ri}_\tau = 120$, and $\mathrm{Ri}_\tau = 480$.

Ri_τ	SSE_{ν_t} [a]	SSE_{κ_t} [b]
60	2.55×10^{-5}	1.34×10^{-5}
120	1.77×10^{-5}	2.71×10^{-6}
480	3.19×10^{-5}	1.06×10^{-6}

[a]Sum of square errors SSE = $\sum$(DNS data - analytical expression)^2 for ν_t.
[b]SSE for κ_t.

to which the conditions below are added on both walls:

$$\hat{u} = \hat{v} = \hat{w} = \hat{T} = 0.$$

These equations represent the primitive form of the stability problem which can be compactly written as

$$\mathcal{L}(\alpha, \beta, \omega, \overline{u})\hat{q}(y, \alpha, \beta, \omega) = 0, \tag{17}$$

where $\mathcal{L}$ is the linear operator of the eigenvalue problem and $\hat{q} = (\hat{u}, \hat{v}, \hat{w}, \hat{T}, \hat{p})^T$.

There are two possible approaches to solve the eigenvalue problem: a temporal one and a spatial one [29]. In this study we have used a temporal approach where the wavenumbers are real and fixed while ω is complex:

$$[\mathcal{A} - \omega\mathcal{B}]\hat{q}(y, \alpha, \beta, \omega) = 0. \tag{18}$$

The asymptotic evolution of a perturbation of the mean state is thus dictated by the sign of $\mathcal{I}(\omega)$, with $\mathcal{I}(\omega) < 0$ corresponding to an exponentially decaying perturbation [30].

The eigenvalue problem is solved numerically with a MATLAB code using a Chebyshev spatial discretization in y, with Dirichlet boundary conditions at both walls [31]. After a grid convergence study, we have chosen a grid consisting of $N_y = 500$ points.

C. Nonmodal stability analysis

In many flow cases, modal stability analysis is not sufficient to describe the full behavior of the fluid system, being limited to its asymptotic dynamics. In fact, an asymptotically stable flow can experience a transient growth of the initial perturbations if their eigenvectors are nonorthogonal. These highly amplified perturbations are dynamically relevant since they often become the most prominent coherent structures populating the flow [22]. Therefore, it is worth to investigate the amplification of the initial perturbation energy over a prescribed time interval.

Since the thermal stratification is stable, the energy is defined as the sum of the L_2 norm of kinetic energy and potential energy. The nondimensional kinetic energy is simply given by the scalar product of the velocity vector with itself while for the nondimensional potential energy we used the relation proposed by Biau and Bottaro [8]:

$$E(t) = \int_V (E_k + E_p)dV = \int_V \frac{1}{2}\left(|\mathbf{u}'(t)|^2 + \frac{\mathrm{Ri}}{\left|\frac{d\overline{T}}{dy}\right|}|T'(t)|^2\right)dV. \tag{19}$$

This formulation of the norm is not trivial, but it arises from physical considerations. In fact, using the Boussinesq hypothesis, the potential energy can be written as

$$E_p = -\rho' g\, dy = \rho_0 \alpha T' g\, dy.$$

Now considering the dimensionless variables

$$\hat{T} = \frac{T'}{\Delta T}, \quad \hat{dy} = \frac{dy}{h},$$

it is possible to obtain a dimensionless formulation for the potential energy by exploiting the Richardson number, as

$$\hat{E}_p = \frac{E_p}{\rho_0 U_0^2} = \frac{\rho_0 \alpha \hat{T} \Delta T \hat{dy} h \mathrm{Ri} U_0^2}{\rho_0 U_0^2 \alpha \Delta T h} = \mathrm{Ri} \hat{T} \hat{dy}.$$

If we consider $\frac{dT_0}{dy} \approx \frac{\hat{T}}{\hat{dy}}$ and we multiply and divide $\hat{E}_p$ for $\hat{T}^2$ in order to obtain a quadratic formulation for the potential energy, we obtain the expression used in Eq. (19).

A priori, it is not possible to define which method is the best for optimizing this objective function. The singular value decomposition (SVD), which has been widely used in the literature [16,26], has the advantage to allow for computing both optimal and suboptimal singular values. However, as discussed in Ref. [32], if the objective function of the optimization is defined by a seminorm or a norm for which not all terms have the same weight, the optimization of gain defined by such a nontrivial seminorm would require a special treatment of further constraints that cannot be imposed by the SVD. However, this can easily be done using variational methods such as constrained optimization with Lagrangian multipliers [33]. These methods are flexible and powerful, since one can optimize for an infinite number of constraints or cost functions, despite an increased complexity and effort in computation and implementation. Thus, in this work we use a Lagrange multiplier framework along with a *direct-adjoint method* in order to find the optimal initial condition that maximizes the growth of energy at a fixed target time T_{opt} [22,34,35]. The Lagrange functional is defined as the energy at target time, subject to the following constraints: the optimal initial perturbation $\mathbf{u}'(0)$ must (i) be divergence free, (ii) be a solution of the linearized Navier-Stokes equation, and (iii) have the energy density norm equal to unity (only for numerical purposes, since we tackle a linear problem). Once these constraints have been set, it is possible to define the Lagrange functional as

$$\begin{aligned}
&\mathcal{L}(\mathbf{u}', T', p', \mathbf{u}^\dagger, T^\dagger, p^\dagger, \mathbf{u}'(0), \mathbf{u}'(T_{\mathrm{opt}}), T'(0), T'(T_{\mathrm{opt}})) \\
&\quad = E(T_{\mathrm{opt}}) - \int_V \int_0^{T_{\mathrm{opt}}} \mathbf{u}^\dagger \cdot \left(\frac{\partial \mathbf{u}'}{\partial t} + (\mathbf{u} \cdot \nabla)\overline{\mathbf{u}} + (\overline{\mathbf{u}} \cdot \nabla)\mathbf{u}' + \nabla p' \right. \\
&\qquad \left. - \frac{1}{\mathrm{Re}} [\nabla \overline{\nu}_t \cdot (\nabla \mathbf{u}' + \nabla \mathbf{u}'^T) + \overline{\nu}_T \nabla^2 \mathbf{u}'] + \mathrm{Ri} T' \mathbf{e}_y \right) dt\, dV \\
&\qquad - \int_V \int_0^{T_{\mathrm{opt}}} T^\dagger \left(\frac{\partial T'}{\partial t} + (\mathbf{u}' \cdot \nabla)\overline{T} + (\overline{\mathbf{u}} \cdot \nabla)T' - \frac{1}{\mathrm{RePr}} (\nabla \overline{\kappa}_t \cdot \nabla T' + \overline{\kappa}_T \nabla^2 T') \right) dt\, dV \\
&\qquad - \int_V \int_0^{T_{\mathrm{opt}}} p^\dagger (\nabla \cdot \mathbf{u}') dV - E^\dagger (E(0) - E_0),
\end{aligned}$$

where $E(T_{\mathrm{opt}})$ is the objective function and the following terms are the momentum equation, the temperature equation, the continuity equation, and the unit norm constraint, respectively, multiplied by the Lagrange multipliers (or adjoint variables) $\mathbf{u}^\dagger$, $T^\dagger$, $p^\dagger$, and $E^\dagger$. To obtain the optimal solution is it necessary to nullify the variations of the Lagrange functional, with respect to each variable, as

follows:

$$\frac{\partial \mathcal{L}}{\partial \mathbf{u}^\dagger} = 0 \rightarrow \frac{\partial \mathbf{u}'}{\partial t} + (\mathbf{u}\cdot\nabla)\overline{\mathbf{u}} + (\overline{\mathbf{u}}\cdot\nabla)\mathbf{u}' = \nabla p' + \frac{1}{\mathrm{Re}}[\nabla\overline{\nu}_t\cdot(\nabla\mathbf{u}' + \nabla\mathbf{u}'^T) + \overline{\nu}_T\nabla^2\mathbf{u}'] + \mathrm{Ri}T'\mathbf{e}_y = 0, \tag{20}$$

$$\frac{\partial \mathcal{L}}{\partial p^\dagger} = 0 \rightarrow \nabla\cdot\mathbf{u}' = 0, \tag{21}$$

$$\frac{\partial \mathcal{L}}{\partial T^\dagger} = 0 \rightarrow \frac{\partial T'}{\partial t} + (\mathbf{u}'\cdot\nabla)\overline{T} + (\overline{\mathbf{u}}\cdot\nabla)T' = \frac{1}{\mathrm{RePr}}(\nabla\overline{\kappa}_t\cdot\nabla T' + \overline{\kappa}_T\nabla^2 T') = 0, \tag{22}$$

$$\frac{\partial \mathcal{L}}{\partial u'} = 0 \rightarrow \frac{\partial u^\dagger}{\partial t} + \overline{u}\frac{\partial u^\dagger}{\partial x} + \frac{1}{\mathrm{Re}}\left[\frac{d\overline{\nu}_t}{dy}\frac{\partial u^\dagger}{\partial y} + \overline{\nu}_T\left(\frac{\partial^2 u^\dagger}{\partial x^2} + \frac{\partial^2 u^\dagger}{\partial y^2} + \frac{\partial^2 u^\dagger}{\partial z^2}\right)\right] + \frac{\partial p^\dagger}{\partial x} = 0, \tag{23}$$

$$\frac{\partial \mathcal{L}}{\partial v'} = 0 \rightarrow \frac{\partial v^\dagger}{\partial t} - u^\dagger\frac{d\overline{u}}{dy} + \overline{u}\frac{\partial v^\dagger}{\partial x} + \frac{1}{\mathrm{Re}}\left[2\frac{d\overline{\nu}_t}{dy}\frac{\partial v^\dagger}{\partial y} + \overline{\nu}_T\left(\frac{\partial^2 v^\dagger}{\partial x^2} + \frac{\partial^2 v^\dagger}{\partial y^2} + \frac{\partial^2 v^\dagger}{\partial z^2}\right)\right] - T^\dagger\frac{d\overline{T}}{dy} + \frac{\partial p^\dagger}{\partial y} = 0, \tag{24}$$

$$\frac{\partial \mathcal{L}}{\partial w'} = 0 \rightarrow \frac{\partial w^\dagger}{\partial t} + \overline{u}\frac{\partial w^\dagger}{\partial x} + \frac{1}{\mathrm{Re}}\left[\frac{d\overline{\nu}_t}{dy}\frac{\partial w^\dagger}{\partial y} + \overline{\nu}_T\left(\frac{\partial^2 w^\dagger}{\partial x^2} + \frac{\partial^2 w^\dagger}{\partial y^2} + \frac{\partial^2 w^\dagger}{\partial z^2}\right)\right] + \frac{\partial p^\dagger}{\partial z} = 0, \tag{25}$$

$$\frac{\partial \mathcal{L}}{\partial p'} = 0 \rightarrow \nabla\cdot\mathbf{u}^\dagger = 0, \tag{26}$$

$$\frac{\partial \mathcal{L}}{\partial T'} = 0 \rightarrow \frac{\partial T^\dagger}{\partial t} + (\overline{\mathbf{u}}\cdot\nabla)T' + \frac{1}{\mathrm{RePr}}(\nabla T^\dagger\cdot\nabla\overline{\kappa}_t + \overline{\kappa}_T\nabla^2 T^\dagger) + \mathrm{Ri}v^\dagger = 0, \tag{27}$$

$$\frac{\partial \mathcal{L}}{\partial E^\dagger} = 0 \rightarrow E(0) = E_0, \tag{28}$$

$$\frac{\partial \mathcal{L}}{\partial \mathbf{u}'(0)} = 0 \rightarrow \mathbf{u}^\dagger(0) - \lambda\mathbf{u}'(0) = 0, \tag{29}$$

$$\frac{\partial \mathcal{L}}{\partial T'(0)} = 0 \rightarrow T^\dagger(0) - \lambda\frac{\mathrm{Ri}}{\left|\frac{d\overline{T}}{dy}\right|}T'(0) = 0, \tag{30}$$

$$\frac{\partial \mathcal{L}}{\partial \mathbf{u}'(T_{\mathrm{opt}})} = 0 \rightarrow \mathbf{u}'(T_{\mathrm{opt}}) - \mathbf{u}^\dagger(T_{\mathrm{opt}}) = 0, \tag{31}$$

$$\frac{\partial \mathcal{L}}{\partial T'(T_{\mathrm{opt}})} = 0 \rightarrow \frac{\mathrm{Ri}}{\left|\frac{d\overline{T}}{dy}\right|}T'(T_{\mathrm{opt}}) - T^\dagger(T_{\mathrm{opt}}) = 0. \tag{32}$$

Equations (20)–(22) are the direct Navier-Stokes equations, while Eqs. (23)–(27) are the adjoint Navier-Stokes equations. Equation (28) imposes the unit-norm constraint for the initial condition, while Eqs. (31) and (32) represent the compatibility condition and Eqs. (29) and (30) are the gradient, needed for the optimization loop.

During the optimization cycle, the direct equations are integrated in time using a given initial condition. At time $t = T_{\mathrm{opt}}$, the final condition for the direct problem is converted into an initial condition for the adjoint problem through the compatibility condition. Then, the adjoint equations are integrated backward in time. At time $T = 0$ the adjoint variables are used to compute the gradient and update the initial condition in the direction of the gradient by means of a gradient-based approach. This direct-adjoint loop is repeated until it converges to the optimal initial condition.

This direct-adjoint cycle is solved numerically. For time integration a fully implicit fourth-order backward Euler scheme is used. The spatial discretization is the same used for the modal analysis, with $N_y = 130$ collocation points. To solve the optimization problem, both the power iteration method and the gradient rotation method [36] with an update angle $\alpha = \pi/12$ are used. Figure 4

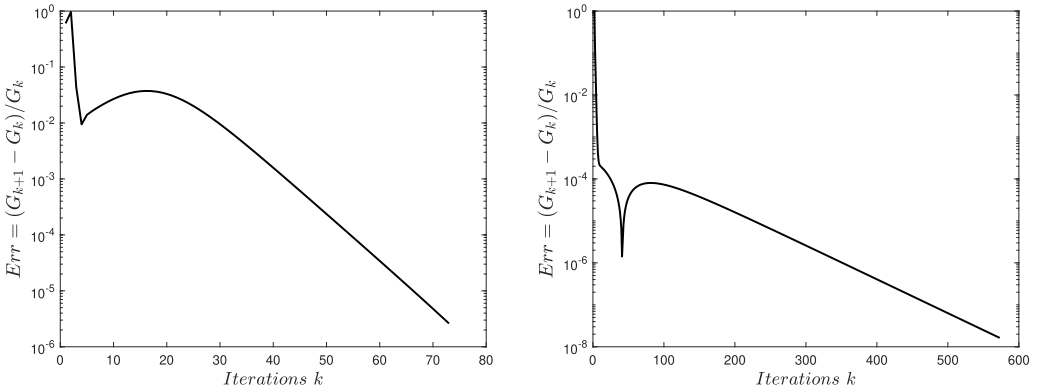

FIG. 4. Convergence study for optimal cases at $\mathrm{Ri}_\tau = 60$, $(\alpha, \beta) = (0, 2.2)$ (left) and $\mathrm{Ri}_\tau = 480$, $(\alpha, \beta) = (0, 6)$ (right).

shows the convergence of the optimization method. Two cases were considered: the first at $\mathrm{Ri}_\tau = 60$, $\alpha = 0$, $\beta = 2.2$, and $T_{\mathrm{opt}} = 34.5$ and the second at $\mathrm{Ri}_\tau = 480$, $\alpha = 0$, $\beta = 6$, and $T_{\mathrm{opt}} = 9.9$. It can be observed that when the effect of stratification increases, the convergence becomes slower.

III. RESULTS

For validating the code, we first considered the stratified and unstratified Poiseuille flow. On this type of configuration, we performed both modal and nonmodal analysis, finding a very good agreement with respect to those of Parente *et al.* [10].

Then, for further validation, we considered the case of turbulent, unstratified channel flow. The reference study in this case was that of Pujals *et al.* [16]. In agreement with Pujals *et al.*'s results, it was found that the flow is asymptotically stable for every Re_τ, and that the energy gain has two peaks, a first one at low β values related to the lift-up mechanism acting at the outer scale, and a second one at higher β values related to the same mechanism at the inner scale (more details in Appendix A). Table IV compares the values we obtained with those of Pujals *et al.* [16].

Once the code was validated, we considered the turbulent stratified channel flow at $\mathrm{Ri}_\tau = 60$, 120, and 480. Modal analysis has been first performed by varying the value of the two wavenumbers. The flow always remains asymptotically stable for all β and α. Three spectra are reported in Fig. 5, for the three considered values of Ri_τ and $\alpha = 2$, $\beta = 2$.

The shape of the spectra is very similar to that of the unstratified turbulent case with a main branch that diverges to the right as α increases. However, it can be observed that when Ri_τ increases, the main branch moves to lower growth rates, while the amplification rate ω_i of the less stable isolated modes reaches higher values than in the previous cases, moving from $\omega_i = -0.0228$ for $\mathrm{Ri}_\tau = 60$ to $\omega_i = -0.0139$ for $\mathrm{Ri}_\tau = 480$. This is in agreement with the work of Garcia-Villalba and Del Alamo [21], which reports the flow becoming linearly unstable for values of $\mathrm{Ri}_\tau \approx 2 \times 10^4$, leading to relaminarization of the flow.

TABLE IV. Values of the spanwise wavenumber related to the outer peak and inner peak optimal perturbations.

	Pujals *et al.* [16] (unstratified)	$\mathrm{Ri}_\tau = 0$	$\mathrm{Ri}_\tau = 60$	$\mathrm{Ri}_\tau = 120$	$\mathrm{Ri}_\tau = 480$
Outer peak β	1.5707	1.5989	1.699	2.597	6
Inner peak β (β^+)	34.17(0.0683)	32.5(0.065)	30.25(0.055)	26.75(0.0486)	

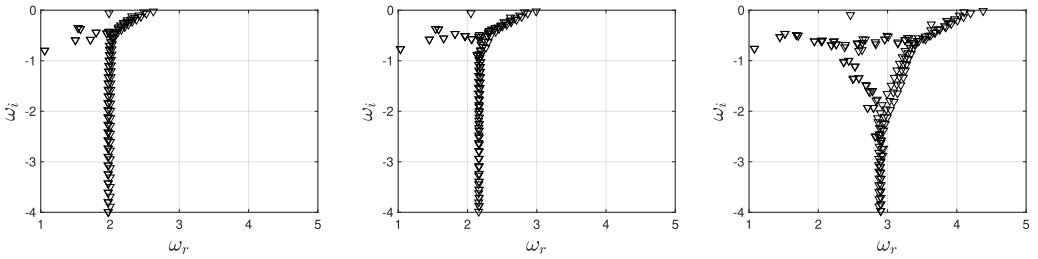

FIG. 5. Eigenspectra for $\mathrm{Ri}_\tau = 60$ ($\mathrm{Ri} = 0.139878$) (left), $\mathrm{Ri}_\tau = 120$ ($\mathrm{Ri} = 0.2797757$) (middle), and $\mathrm{Ri}_\tau = 480$ ($\mathrm{Ri} = 1.11910287$) (right) for $\mathrm{Re}_\tau = 550$ ($\mathrm{Re} = 11390.6$), $\alpha = 2$, and $\beta = 2$.

Due to the fact that the considered flow configurations are asymptotically stable, we now tackle nonmodal analysis. Since for the laminar stratified channel and boundary layer flows [10,28] the optimal perturbation occurs for nonzero values of the streamwise wavenumber, we have computed the maximum energy gain for $\alpha \in [0, 4]$ and $\beta \in [0, 4]$ in the cases $\mathrm{Ri}_\tau = 60$ and 120 and for $\alpha \in [0, 4]$ and $\beta \in [0, 6]$ in the case $\mathrm{Ri}_\tau = 480$.

The optimal energy gain maps in Fig. 6 show that, for all the three considered values of Ri_τ, the maximum energy value occurs at $\alpha = 0$, similarly to the unstratified turbulent channel flow [16], but differently from the laminar stably stratified channel flow [10,28]. Thus, for assessing the effects of stratification on the transient energy growth in a turbulent channel, we first consider the optimal case with $\alpha = 0$. We investigate the optimal energy growth by setting $\alpha = 0$ and different values of the spanwise wavenumber β varying from 0 to 500. The optimal energy gain for each β and Ri_τ value is shown in the left frame of Fig. 7. It can be observed that by increasing the stratification of the flow, the energy gain at the outer peak increases by two orders of magnitude. In particular, the peak values of the optimal energy gain increase with Ri_τ as shown in the right frame of Fig. 7, following a power law of the type $G_{\max} = a\mathrm{Ri}_\tau^b + c$ with $a = 0.03285$, $b = 1.967$, and $c = 9.81$. This indicates that a strong stable stratification considerably increases the strength of large-scale coherent structures within the turbulent flow. Notice that this simply means that the operator in the stratified case is more non-normal, and therefore exhibits more energy growth during transients. However, nothing can be said about the role of stratification in the persistence of large-scale coherent structures at longer times, a nonlinear analysis being beyond the interest of this paper.

Nonetheless, in the left frame of Fig. 7 one can notice that the spanwise wavenumber for which the energy gain peaks (i.e., the *outer* optimal value of β) increases with Ri_τ, reaching four times its unstratified value at the highest Ri_τ considered. The optimal values of β in the three considered cases are reported in Table IV. It is also noteworthy to observe that for the larger value of Ri_τ, the range

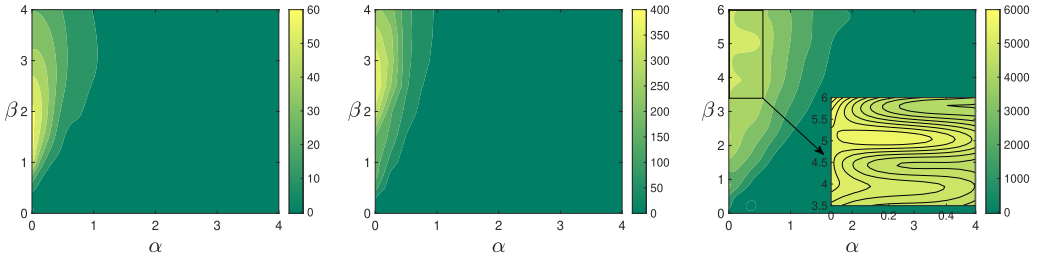

FIG. 6. Contours of $G_{\max}$ in function of α and β for $\mathrm{Ri}_\tau = 60$ (left), $\mathrm{Ri}_\tau = 120$ (middle), and $\mathrm{Ri}_\tau = 480$ (right), where $G_{\max}$ refers to the max value of the gain in time. The values of β used are [1, 1.25, 1.5, 1.75, 2, 2.5, 3, 3.5, 4, 5, 7.5, 10, 12.5, 15, 20, 25, 28, 30, 32, 35, 40, 50, 60, 70, 80, 90, 100, 110, 120, 130, 140, 150, 160, 170, 180, 190, 200, 210, 250, 300, 350, 400, 450, 500].

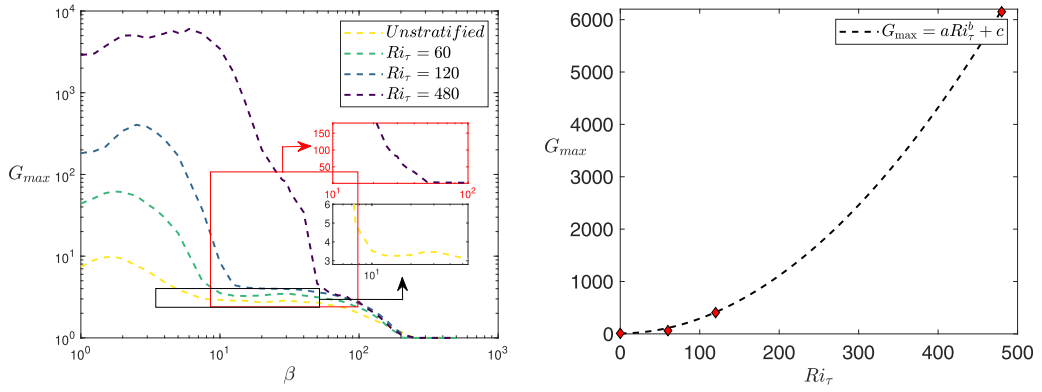

FIG. 7. $G_{\max}$ versus β for different values of Ri_τ (left) and versus Ri_τ for the optimal value of β (right) with $\alpha = 0$ and $\mathrm{Re}_\tau = 550$ ($\mathrm{Re} = 11390.6$). The black and red boxes represent the zoomed-in areas of the plot.

of (small) spanwise wavenumbers allowing a strong energy growth is very large, going from $\beta \approx 1$ to $\beta \approx 6$. It is important to verify whether this optimal spanwise wavenumber range corresponds to that reported in the DNS of stably stratified turbulent channels. In particular, Fig. 18 of Ref. [21] provides two-dimensional spectral densities for different Ri_τ in the "outer" regions, that are found to lie in the range $\beta \in [1, 6]$, closely corresponding to the optimal values of β found in the present analysis. Moreover, they report a peak value of $\lambda_z = 2\pi/\beta \approx 1$, which corresponds to a value of $\beta \approx 6$ as that obtained through our nonmodal analysis for the considered Ri_τ. The present results thus suggest that the strong alterations observed by DNS in the energy-carrying large-scale coherent structures at high Ri_τ may be due to the changes in the transient energy-growth mechanisms induced by the presence of a stable thermal stratification.

At the same time, the value of the optimal gain for the inner peak slightly increases at moderate Ri_τ. One can notice that the inner optimal value of β decreases slightly with Ri_τ and for the case at $\mathrm{Ri}_\tau = 480$ the scale separation is no longer visible; therefore, one can suppose that strong thermal stratification may lead to the disappearance of the scale separation between the inner and the outer amplification dynamics, leading towards an intermediate-scale amplification mechanism, similarly to what is observed in the streamwise spectral energy extracted by the DNS (see Fig. 18a of Ref. [21]). Moreover, inspecting the optimal perturbation profiles at $\mathrm{Ri}_\tau = 0$ and $\mathrm{Ri}_\tau = 60$ provided in Fig. 8 (for $t = 0$) and Fig. 9 (at T_{opt}), it appears that the inner-scale energy-growth mechanism is not affected at all by the presence of stratification, except for the presence of a weak temperature streak. The same conclusion can be drawn when the Richardson number is further increased. This corroborates the observation made through DNS in Ref. [21] that the coherent structures at the wall are not altered by the presence of stable stratification. Since the inner dynamics is not affected by the presence of stratification, in the following we will focus on the effect of the increase of Ri_τ on the large-scale transient growth mechanisms ($\beta \leqslant 6$).

A. Case with $\mathrm{Ri}_\tau = 60$

1. Streamwise-independent perturbations ($\alpha = 0$)

At $\mathrm{Ri}_\tau = 60$, the global optimum is observed at $\alpha = 0$ and $\beta = 1.699$, generating at optimal time velocity streaks. For these wavenumbers the maximum value of the gain achieved is $G_{\max} = 61.95$ at time $T_{\max} = 34.5$, and the energy gain curve presents one single peak, as shown in Fig. 10 (left frame). This maximum energy value is larger than that reported in the turbulent unstratified case, due to the growth of potential energy. Analyzing the real and imaginary parts of the initial perturbation that leads to the above-mentioned energy gain $G_{\max}$ in Fig. 11, one can notice that at initial time the perturbation consists of positive and negative temperature fluctuations and spanwise rolls, which

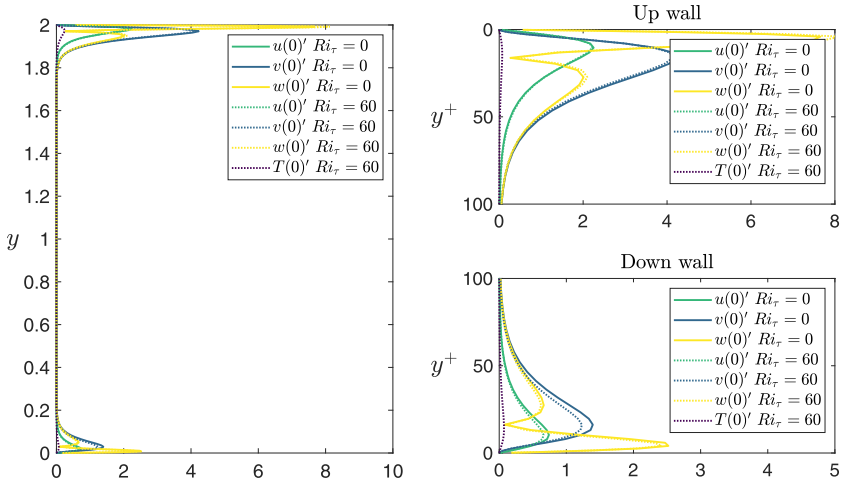

FIG. 8. Module of the optimal perturbation at time $t = 0$ for the inner peak at $\mathrm{Ri}_\tau = 0$ and $\mathrm{Ri}_\tau = 60$ (see Table IV).

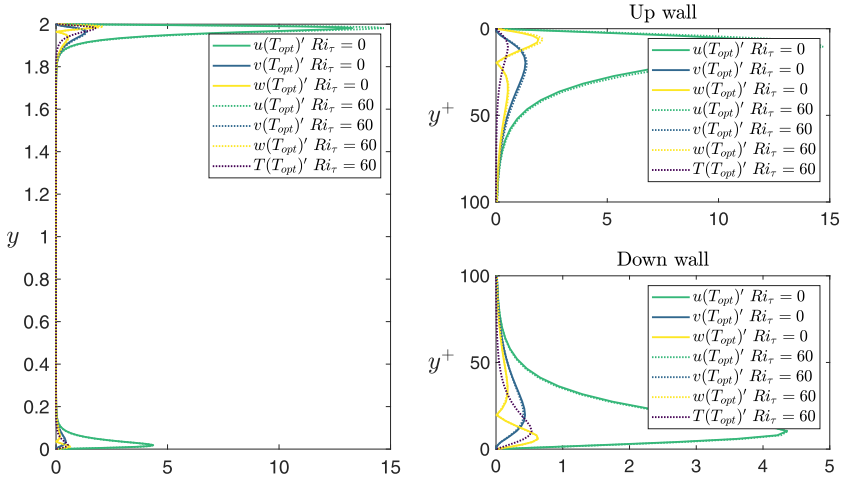

FIG. 9. Module of the optimal perturbation at time $t = T_{\mathrm{opt}}$ for the inner peak at $\mathrm{Ri}_\tau = 0$ and $\mathrm{Ri}_\tau = 60$ (see Table IV).

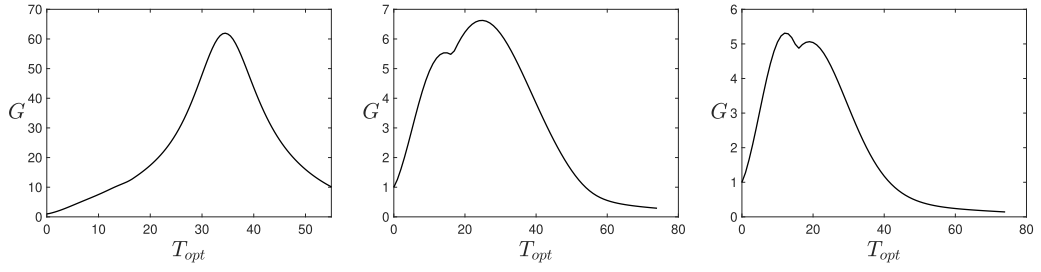

FIG. 10. Optimal energy gain versus target time at $\mathrm{Ri}_\tau = 60$ for $\alpha = 0$, $\beta = 1.699$ (left), $\alpha = 0.5$, $\beta = 1$ (middle), and $\alpha = 0.75$, $\beta = 1$ (right).

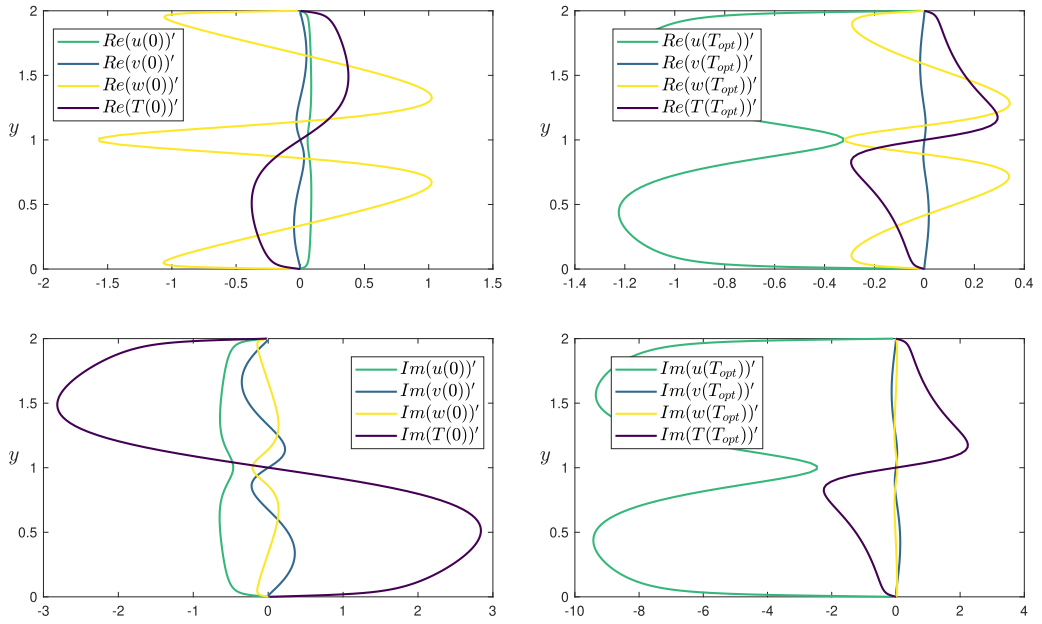

FIG. 11. Real part (upper frames) and imaginary part (lower frames) of the optimal perturbation at time $t = 0$ (left) and at time $t = T_{\text{opt}} = T_{\text{max}}$ (right) for $\alpha = 0$, $\beta = 1.699$, and $\text{Ri}_\tau = 60$.

become velocity streaks at target time. Thus, a double transfer of energy occurs, at first due to the coupling of temperature and velocity terms in the equations and then to the classical *lift-up* mechanism. Thus, due to the temperature-velocity coupling, the energy-production mechanism on which the self-sustaining cycle of turbulence is grounded appears to be overall enhanced by the presence of stable stratification, at least in the range of Richardson numbers considered in this study.

2. *Streamwise-dependent perturbations ($\alpha \neq 0$)*

In order to gain an insight on other possible energy-growth mechanisms within the considered flow, we extend our analysis of the transient energy growth at nonzero values of the streamwise wavenumbers. When analyzing the optimal energy gain versus the target time in Fig. 10 (middle and right frames) for two different nonzero values of α and $\text{Ri}_\tau = 60$, one can observe that the energy gain curve has two peaks, probably related to switch between two singular values.

In order to investigate this point, we analyze in Fig. 12 the wall-normal profiles of the velocity and temperature components for the optimal perturbation at target time for the two cases shown in Fig. 10. In the first case ($\alpha = 0.5$, $\beta = 1$) the global optimum is that at larger target times (see the middle frame of Fig. 10). As shown in the left frames of Fig. 12, this transient energy growth leads at the optimal time to streamwise-velocity streaks characterized by a wall-normal symmetry, recalling the classical lift-up mechanism present in unstratified channel flow [37,38]. Compared to the optimal mechanism found for $\alpha = 0$, the temperature streaks appear stronger. Figure 13 shows the optimal perturbation at initial (left) and target (right) time in a cross-stream plane. The vectors show the presence of typical alternated cross-flow rolls that transport the base flow shear to create streamwise velocity and temperature fluctuations. While at initial time the temperature perturbation is spread in the whole domain, at target time it localized in the vicinity of the core of the channel. Notably, the temperature perturbation is antisymmetric with respect to the center channel, whereas the streamwise velocity perturbations, which are shown in the x-y plane in Fig. 14 (left for initial time, right for target time), are characterized by wall-normal symmetry. Moreover,

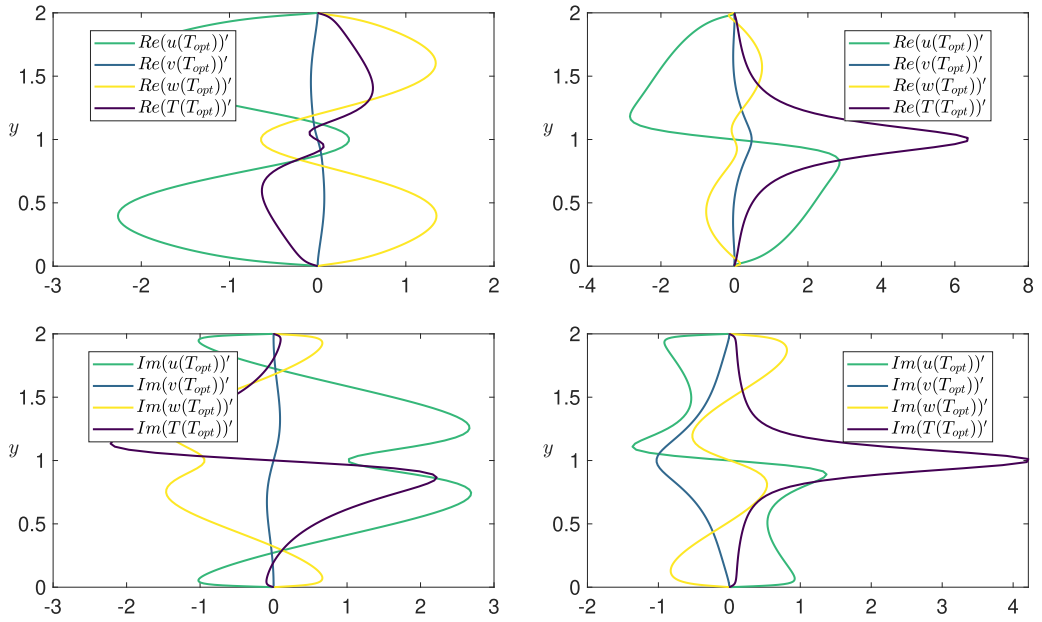

FIG. 12. Real part (upper frames) and imaginary part (lower frames) of the optimal perturbation at $\mathrm{Ri}_\tau = 60$ for cases $\alpha = 0.5$, $\beta = 1$, $t = T_{\mathrm{opt}} = 25$ (left) and $\alpha = 0.75$, $\beta = 1$, $t = T_{\mathrm{opt}} = 12$ (right).

the velocity disturbances are not localized in the wall-normal direction, but their orientation changes from upwards to downwards in time, suggesting that the Orr mechanism is acting as well [10,39].

However, in the second case ($\alpha = 0.75$, $\beta = 1$), whose energy growth is shown in the right frame of Fig. 10, the global optimum occurs at shorter target times and leads at the optimal time to a center-channel temperature peak accompanied by weaker antisymmetric velocity streaks (see right frames of Fig. 12). Figures 15 and 16 show the optimal perturbation at initial (left) and target (right) time in two cross sections. Again, some cross-flow rolls that transport the base flow shear to create temperature fluctuations can be seen. However, the temperature perturbations are now symmetric with respect to the center channel, while they appeared to be antisymmetric in

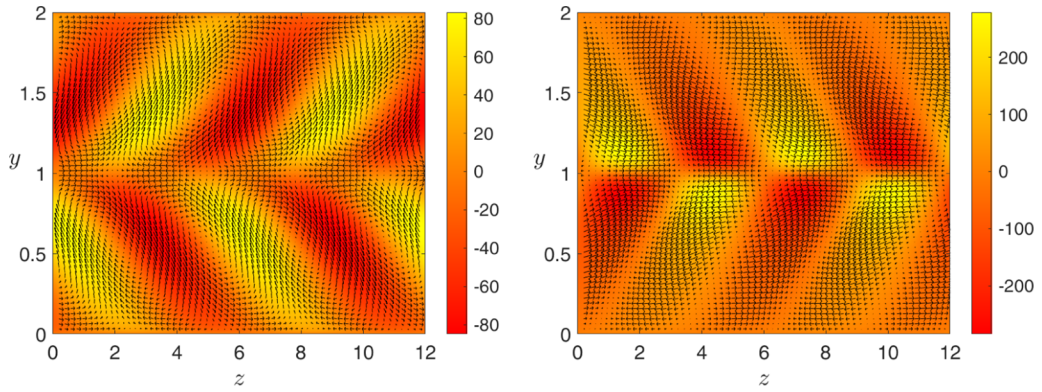

FIG. 13. Real part of the optimal perturbation at time $t = 0$ (left) and $t = T_{\mathrm{opt}}$ (right) for $\alpha = 0.5$, $\beta = 1$, and $\mathrm{Ri}_\tau = 60$ in the plane z-y. Shaded contours of temperature and vectors of $w' - v'$.

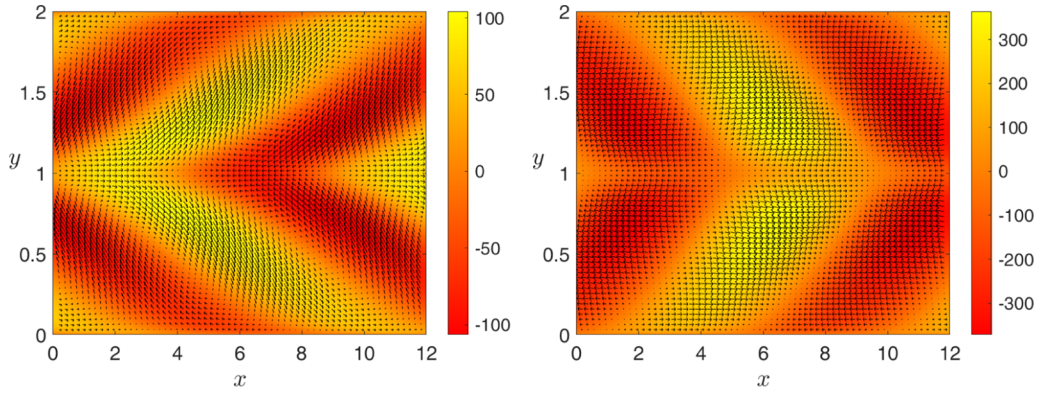

FIG. 14. Real part of the optimal perturbation at time $t = 0$ (left) and $t = T_{\text{opt}}$ (right) for $\alpha = 0.5$, $\beta = 1$, and $\text{Ri}_\tau = 60$ in the plane x-y. Shaded contours of u' and vectors of $u' - v'$.

the previous case. At target time, the temperature fluctuations are localized exactly in the center channel.

As one can observe from Fig. 10, the gain associated to these two mechanisms is comparable, and changing the streamwise and spanwise wavenumbers the global optimum switches from one mechanism to the other. A map showing the α and β values for which the global optimum changes between these two mechanisms is shown in Fig. 17. For each value at the left of the continuous line, the stronger amplification mechanism leads to wall velocity streaks, while on the right-most side of the curve the main transient growth mechanism is related to the generation of a central temperature streak.

In general, it can be observed that for $\alpha < \beta$ the lift-up mechanism prevails whereas for $\beta > \alpha$ the centerline-temperature mechanism dominates the growth, while for $\alpha \geqslant 1.5$ only the latter mechanism is observed.

In order to gain an insight on the mechanisms ensuring the energy growth in these two distinct cases, we evaluate the energy exchange by using a generalized version of the Reynolds-Orr equation, which is currently used in the literature for evaluating the contributions of dissipation and kinetic energy production in the unstratified laminar case. Thus, we scalarly multiply Eq. (6b) by $\mathbf{u}'$ and Eq. (6c) by T'. The resulting equations are then integrated over the entire volume, resulting in the

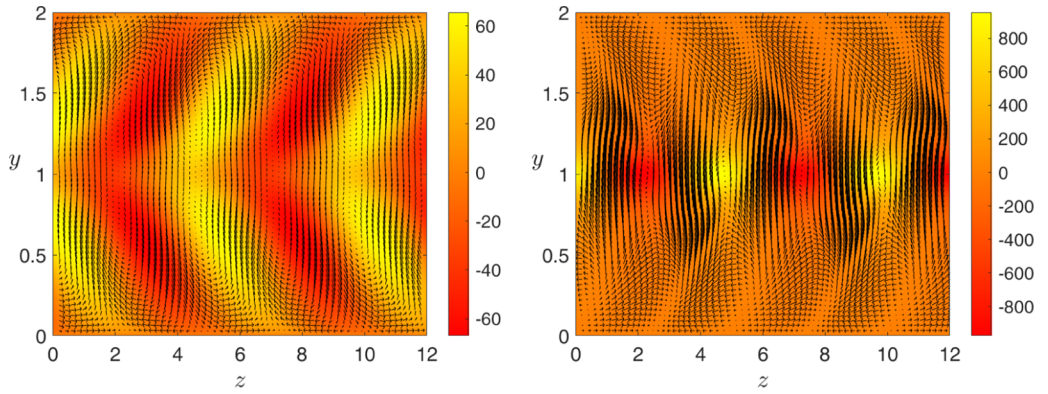

FIG. 15. Real part of the optimal perturbation at time $t = 0$ (left) and $t = T_{\text{opt}}$ (right) for $\alpha = 0.75$, $\beta = 1$, and $\text{Ri}_\tau = 60$ in the plane z-y. Shaded contours of temperature and vectors of $w' - v'$.

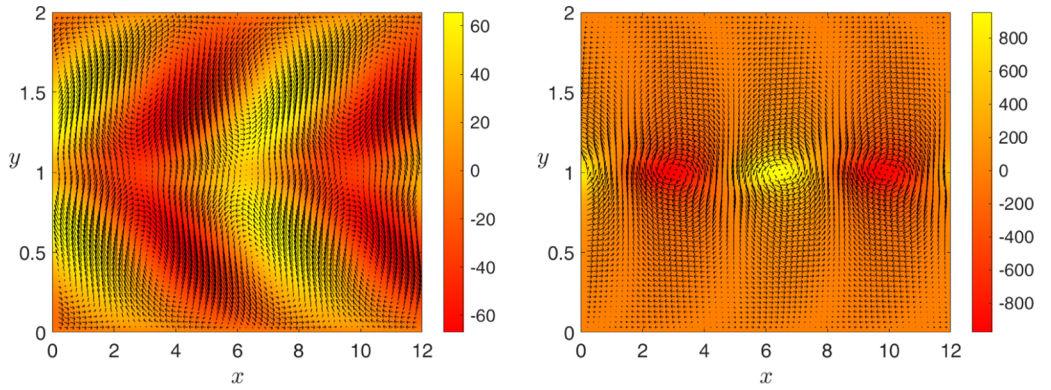

FIG. 16. Real part of the optimal perturbation at time $t = 0$ (left) and $t = T_{\text{opt}}$ (right) for $\alpha = 0.75$, $\beta = 1$, and $\text{Ri}_\tau = 60$ in the plane x-y. Shaded contours of temperature and vectors of $u' - v'$.

modified Reynolds-Orr equations composed of the different terms:

$$\frac{dE_k}{dt} = \underbrace{-\int_V (\mathbf{u}' \cdot (\mathbf{u}' \cdot \nabla)\overline{\mathbf{u}})dV}_{P_u} \underbrace{-\int_V \frac{1}{\text{Re}}\overline{\nu}_T(\nabla\mathbf{u}' : \nabla\mathbf{u}')dV}_{D_u+D_v+D_w} + \underbrace{\int_V \frac{1}{\text{Re}}(\nabla\overline{\nu}_t \cdot (\mathbf{u}' \cdot \nabla)\mathbf{u}')dV}_{Tur}$$

$$\underbrace{+\,\text{Ri}\int_V (T'\mathbf{u}' \cdot \mathbf{e}_y)dV}_{P_{ut}}, \tag{33}$$

$$\frac{dE_p}{dt} = \underbrace{-\int_V (T'(\mathbf{u}' \cdot \nabla)\overline{T})dV}_{P_T} \underbrace{-\int_V \frac{1}{\text{RePr}}\overline{\kappa}_T(\nabla T' \cdot \nabla T')dV}_{D_T}. \tag{34}$$

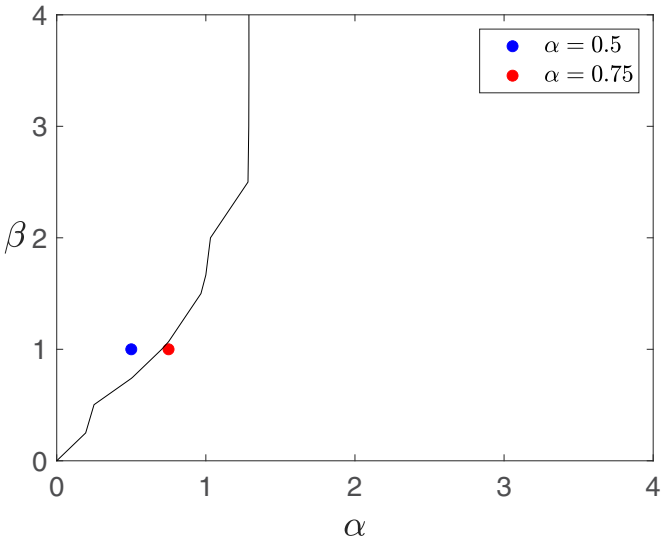

FIG. 17. Values of the spatial wavenumbers for which the optimal energy gain mechanism changes for $\text{Ri}_\tau = 60$. The map is obtained by representing the isovalues of the difference of the two energy peaks: $\Delta G = G_{\text{1st-mech}} - G_{\text{2nd-mech}}$. When $\Delta G > 0$ the first mechanism prevails; when $\Delta G < 0$ the second one dominates. The boundary represents the isovalue at $\Delta G = 0$. The colored dots represent the two flow cases for which the optimal perturbations are discussed in detail.

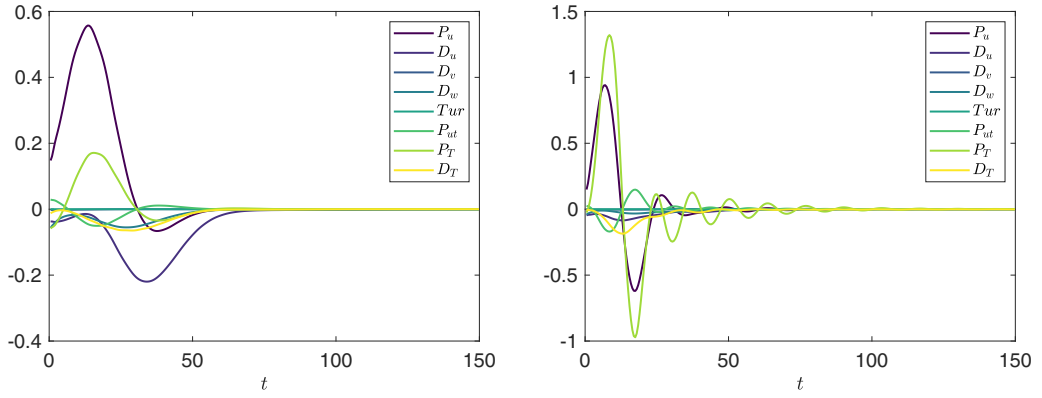

FIG. 18. Energy budget contributions for the optimal mechanism at $\alpha = 0.5$, $\beta = 1$ (left) and for that at $\alpha = 0.75$, $\beta = 1$ (right) for $\mathrm{Ri}_\tau = 60$.

In Eq. (33), which evaluates the variation of the kinetic energy E_k, one can find the classical production term P_u, the dissipation terms $D_u + D_v + D_w$, considering the presence of turbulent viscosity, along with a term taking into account the variation of turbulent viscosity with respect to the wall-normal direction (Tur) and the temperature-velocity coupling term P_{ut} which is the buoyancy flux production. However, the variation of the potential energy is governed only by the temperature production P_T and thermal dissipation D_T [see Eq. (34)].

The time variation of the previously introduced terms is provided in Fig. 18. In the case at smaller α (left frame), the strongest term is that of velocity production, followed by that of temperature production, while the other terms are negative almost during the whole time evolution. The only exception is the temperature-velocity coupling term P_{uT}, which is positive at very short times, indicating that in this early phase the wall-normal velocity fluctuations and the temperature ones have the same sign. Nevertheless, this term decreases when the production terms increase, indicating that the temperature and velocity streaks have opposed sign. However, while the coupling term extracts kinetic energy from the flow, the very large production of kinetic energy and the temperature production term P_T compensate for this effect. This confirms that in this case the amplification mechanism may be linked to a velocity-based mechanism such as the lift-up mechanism, which created high-amplitude velocity and temperature streaky structures (see Ref. [10]).

However, for the larger value of α (right frame), the strongest term is that of temperature production, followed by that of velocity production, indicating that this mechanism is driven by the increase of the potential energy rather than the kinetic one, and it is intimately linked to the presence of stratification. To further corroborate this conjecture, we have performed an optimization removing the term $v' \frac{\partial \overline{T}}{\partial y}$, which is the only energy source of the production term P_T, from the direct temperature equation and its adjoint counterpart $T^\dagger \frac{\partial \overline{T}}{\partial y}$ from the adjoint wall-normal velocity momentum equation. As expected, removing this production term leads to the disappearance of the second energy peak, the only mechanism leading to a possible increase of the energy gain being the classic lift-up mechanism. The results can be observed in Fig. 19. Artificially zeroing the coupling term between velocity and temperature, the energy gain curve presents a single peak related to the lift-up, while the second mechanism disappears. This corroborates the hypothesis that this amplification mechanism is intimately linked to the presence of stratification.

Another noticeable feature of this case is the oscillating trend of the different energy contributions. This behavior is probably related to a beating between the two most important eigenmodes represented in red in Fig. 20, ω_{r1} and ω_{r2}. An interaction between these two modes would lead in this case to an oscillation period $T_- = 2\pi/(\omega_{r1} - \omega_{r2}) \approx 13.48$ which corresponds well to the period of the observed oscillations of term P_T in the right frame of Fig. 18.

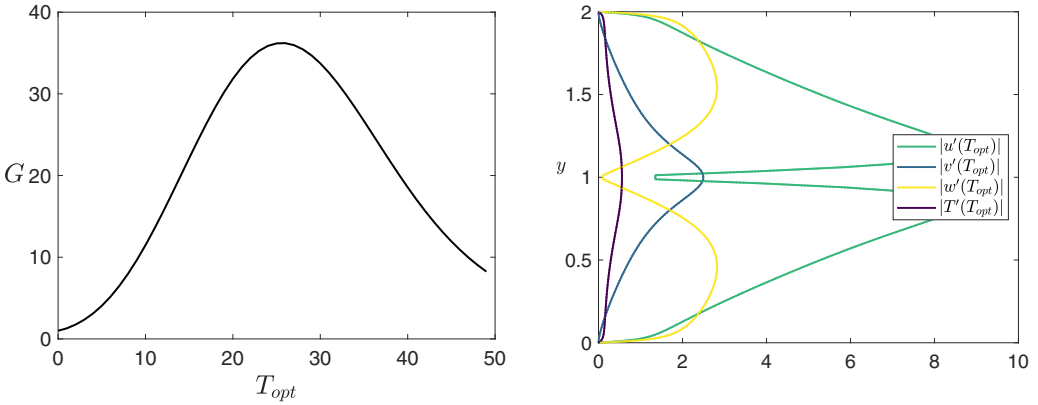

FIG. 19. Optimal energy gain versus target time (left frame) and module of optimal perturbation (right frame) obtained by setting the term $v'\partial\overline{T}/\partial y$ to zero in the temperature equations, as well as its adjoint counterpart in the adjoint wall-normal momentum equation, for the case at $\mathrm{Ri}_\tau = 60$, $\alpha = 0.75$, and $\beta = 1$.

B. Case at $\mathrm{Ri}_\tau = 120$

1. Streamwise-independent perturbations ($\alpha = 0$)

Increasing the value of Ri_τ up to 120, we notice in Fig. 6 that the maximum gain $G_{\max}$ occurs again for $\alpha = 0$. The map is very similar to the low-Ri_τ case although it is slightly shifted to higher values of β and the magnitude of energy is increased by an order of magnitude with respect to the previous case.

However, as shown in Fig. 21, in this case three local maxima are present in the energy gain curves, even for $\alpha = 0$. The first one, which is very weak and associated with very small target times ($T_{\mathrm{opt}} = 6.5$ in Fig. 21), corresponds to the short-time mechanism discussed before, leading to a central temperature streak and two antisymmetric velocity streaks, as shown in the left frame of Figs. 22 and 23 at initial and target time, respectively. The second energy-growth mechanism peaking at intermediate target times ($T_{\mathrm{opt}} = 19.5$ in Fig. 21) corresponds to the lift-up effect, as shown in the middle frame of Figs. 22 and 23 at initial and target time, respectively. The last one, which is the global optimum ($G_{\max} = 405.46$, $T_{\mathrm{opt}} = 23.75$) is due to both kinetic energy and thermal effects and is the first mechanism that returns dominant at long timescales. In fact, at the optimal time (right frame of Fig. 23), it presents two wall velocity streaks which are highly

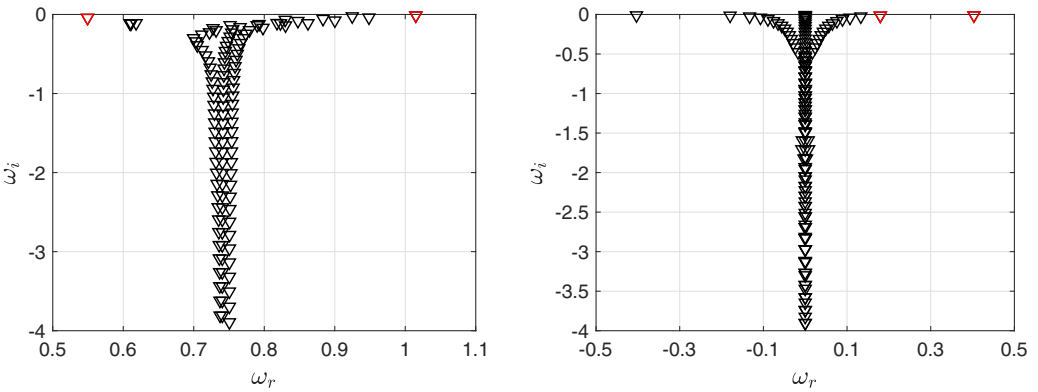

FIG. 20. Eigenspectra for $\mathrm{Ri}_\tau = 60$, $\alpha = 0.75$, $\beta = 1$ (left) and for $\mathrm{Ri}_\tau = 120$, $\alpha = 0$, $\beta = 2.597$ (right).

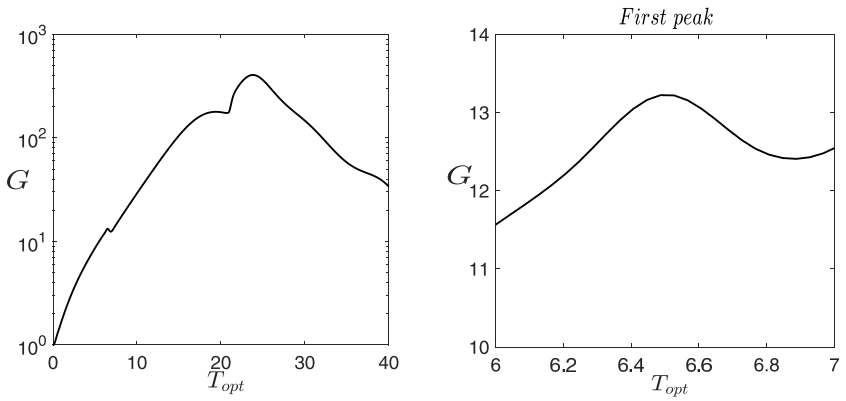

FIG. 21. Optimal energy gain versus T_{opt} for $\alpha = 0$, $\beta = 2.597$ and $\text{Ri}_\tau = 120$ (left) and close-up of the first peak (right).

asymmetrical and have opposite sign in the upper and lower parts of the channel, due to a greater influence of the temperature field which is not symmetrical with respect to the center channel. This asymmetry, already observed for the first peak, is enhanced by a further increase of Ri_τ (see the next section). Similar antisymmetric streaky perturbations have been observed also in the DNS [21], where for a sufficiently high stratification the core of the channel has been found to act as a barrier to turbulent momentum and buoyancy transport, dividing the channel into two virtually separate regions. Furthermore, the initial optimal perturbation related to the third peak presents a small central temperature streak, which for very large times becomes the perturbation term with the largest amplitude as a result of a continuous energy exchange between v' and T' (see Fig. 22).

The contributions of the different production and dissipation terms to the energy growth are thus evaluated for the case leading to the maximum gain. Looking at the left frames of Fig. 24, one can observe that the largest term is that of velocity production. The term of temperature production has also a rather large value, although it strongly oscillates in time, similarly to P_u. This behavior is probably related to a beating of the two less stable eigenmodes (see red symbols in the right frame of Fig. 20), that would lead in the case under consideration to oscillations of period

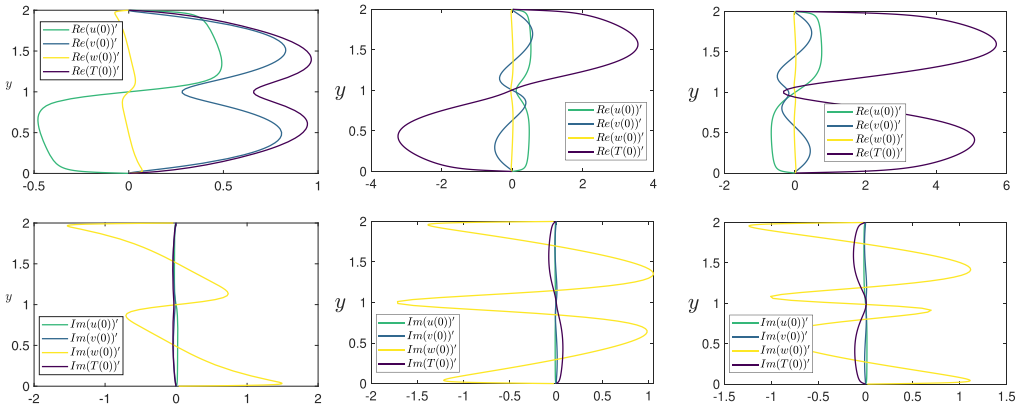

FIG. 22. Real part (upper frames) and imaginary part (lower frames) of the initial optimal perturbations at $t = 0$ for $\alpha = 0$, $\beta = 2.597$, and $\text{Ri}_\tau = 120$ related to the first (left), second (middle), and third (right) energy peaks shown in Fig. 21.

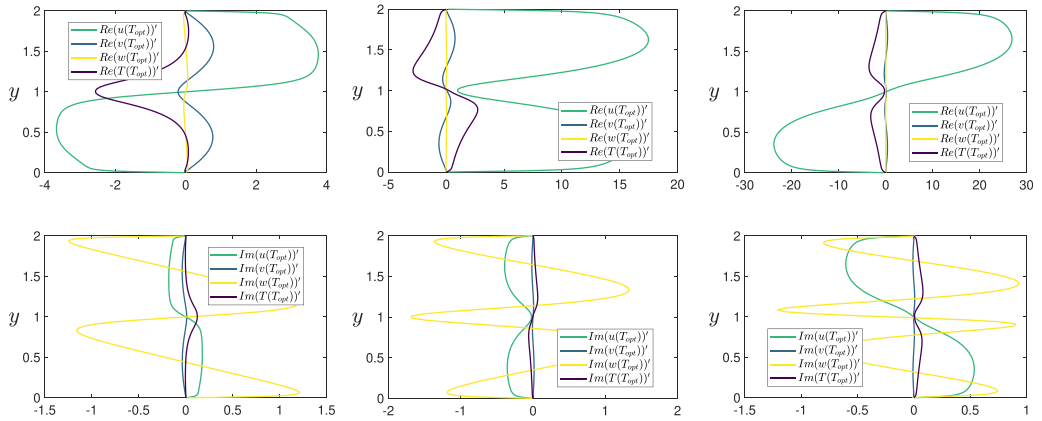

FIG. 23. Real part (upper frames) and imaginary part (lower frames) of the optimal perturbations at $t = T_{\text{opt}}$ for $\alpha = 0$, $\beta = 2.597$, and $\text{Ri}_\tau = 120$ related to the first (left, $T_{\text{opt}} = 6.5$), second (middle, $T_{\text{opt}} = 19.5$), and third (right, $T_{\text{opt}} = 23.75$) energy peaks shown in Fig. 21.

$T_- = 2\pi/(\omega_{r1} - \omega_{r2}) \approx 29$, $T_+ = 2\pi/(\omega_{r1} + \omega_{r2}) \approx 11$, roughly corresponding to those observed in the energy gain curve.

In order to better understand how the energy is exchanged between the different energy production terms during these oscillations, we compute the energy flux in the wall-normal direction, using the approach proposed by Farano *et al.* [40] and Jiménez [41] generalized to the stratified (but linear) case.

Using the Reynolds-Orr equations without integration by parts, we found that the energy flux in the wall-normal direction is (more details in Appendix B)

$$\Phi = v'p'.$$

The latter is integrated with respect to the spanwise and streamwise directions and compared with the main energy terms, i.e., the velocity and temperature production terms

$$P'_U = \int_x \int_z (\mathbf{u}' \cdot (\mathbf{u}' \cdot \nabla)\overline{\mathbf{u}}) dz dx, \tag{35}$$

$$P'_T = \int_x \int_z (T'(\mathbf{u}' \cdot \nabla)\overline{T}) dz dx, \tag{36}$$

for some time instants of interest, in the right frame of Fig. 24. It can be observed that, in the first energy-growth phase, the temperature production term always peaks at the center of the channel, despite having alternating positive and negative values, while the velocity term peaks in a region closer to the walls and is always positive, confirming that the optimal energy-growth mechanism is more driven by convection than by buoyancy. The energy flux is essentially directed towards the center of the channel, being mostly positive (negative) in the lower (upper) part of the channel. Thus, there appears to be a continuous transfer of energy between the velocity and temperature terms, where the energy production is essentially driven by the lift-up mechanism closer to the wall (see the term P_U in the left frame of Fig. 24).

To help the reader understand how the energy transfer occurs, we have solved the system of linearized Navier-Stokes equations imposing as an initial condition the optimal initial perturbations of the case at $\text{Ri}_\tau = 120$ (those in the right-hand frame of Fig. 22). The velocity u' and temperature T' at different times have been represented in Fig. 25. From these temporal snapshots, one can easily observe that a transfer of energy occurs from the temperature at the center of the channel towards the velocity at the wall and vice versa.

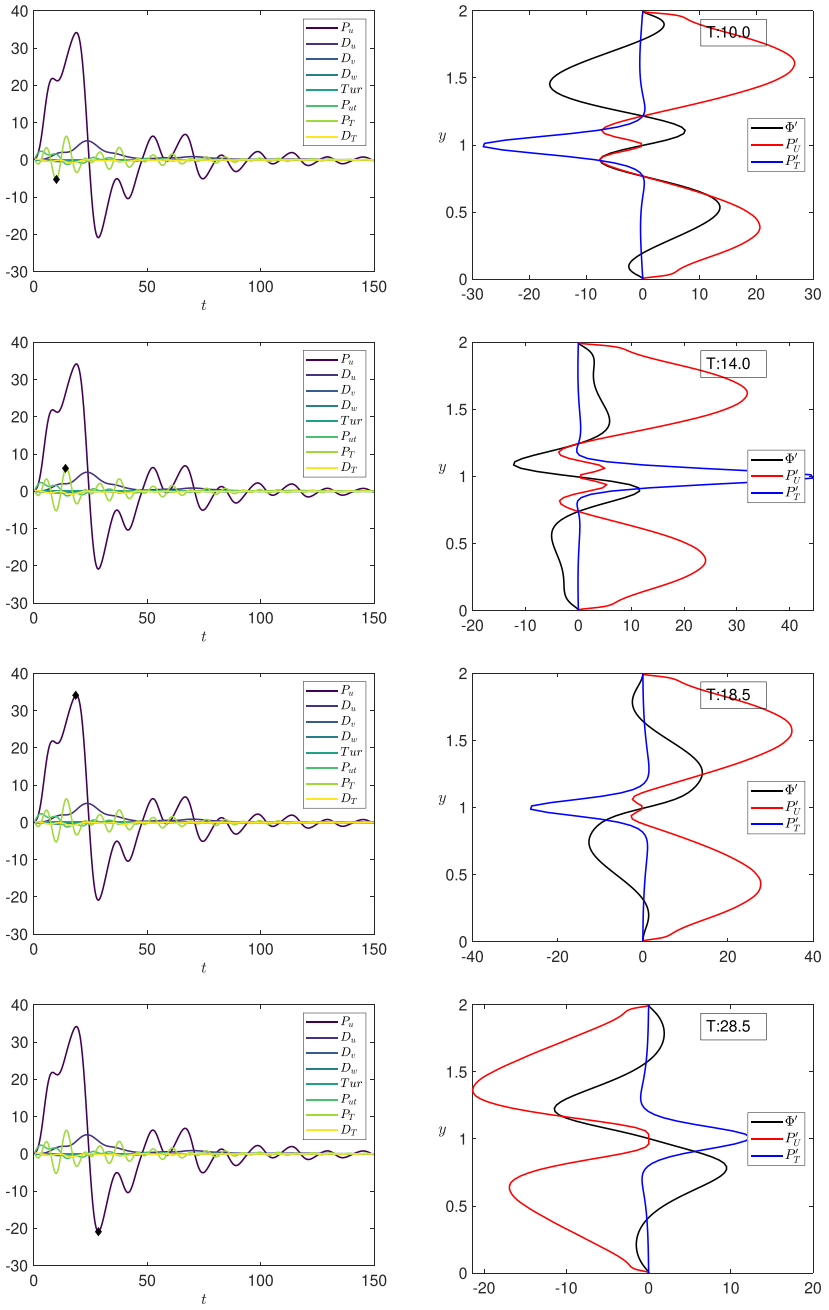

FIG. 24. Energy budget (left) and flux and production (right) for $\mathrm{Ri}_\tau = 120$, $\alpha = 0$, $\beta = 2.597$, and $T_{\mathrm{opt}} = 23.75$. The right plots refer to the time instants identified by the black symbols in the left frames and reported in the legend.

2. Streamwise-dependent perturbations ($\alpha \neq 0$)

As for the case at $\mathrm{Ri}_\tau = 60$, the different energy-growth mechanisms observed at $\alpha = 0$ exist also for nonzero values of α, and become the primary energy-growth mechanisms for given values

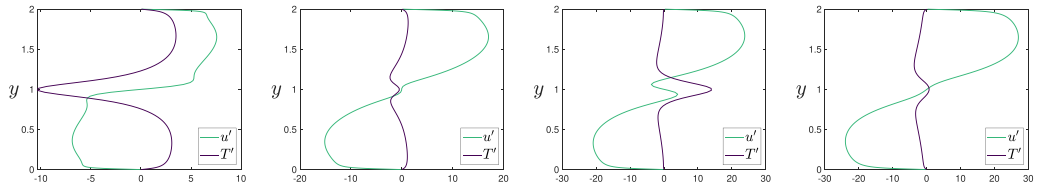

FIG. 25. Time evolution of the optimal streamwise velocity u' and temperature T' perturbations for $\alpha = 0$ and $\beta = 2.597$, at $\mathrm{Ri}_\tau = 120$ at times $T = 5.8$ (left), $T = 11.6$ (left middle), $T = 17.4$ (right middle), and $T = 23.2$ (right).

of the spanwise wavenumber. Inspecting the map in Fig. 26, it appears that for $\alpha > \beta$ the optimal mechanism is the first one generating a temperature streak at the center of the channel, while for $\beta > \alpha$ we rather observe a lift-up-based mechanism inducing velocity streaks at the wall. For values of $\beta \geqslant 1.5$ the first mechanism returns dominant but at a longer time. In order to verify that there is no new mechanism in play, an SVD study for a slightly different norm has been performed which reported the presence of only two singular values that switch over time (more details in Appendix D).

C. Case at $\mathrm{Ri}_\tau = 480$

1. Streamwise-independent perturbations ($\alpha = 0$)

Let us now focus on the largest Richardson number case. Again, the global maximum is obtained for $\alpha = 0$, as shown in the right frame of Fig. 6. Despite that the global optimum is related to the lift-up mechanism, different energy gain mechanisms exist for different values of the target time (as well as for different spatial wavenumbers, as will be shown in the next paragraph). For the case

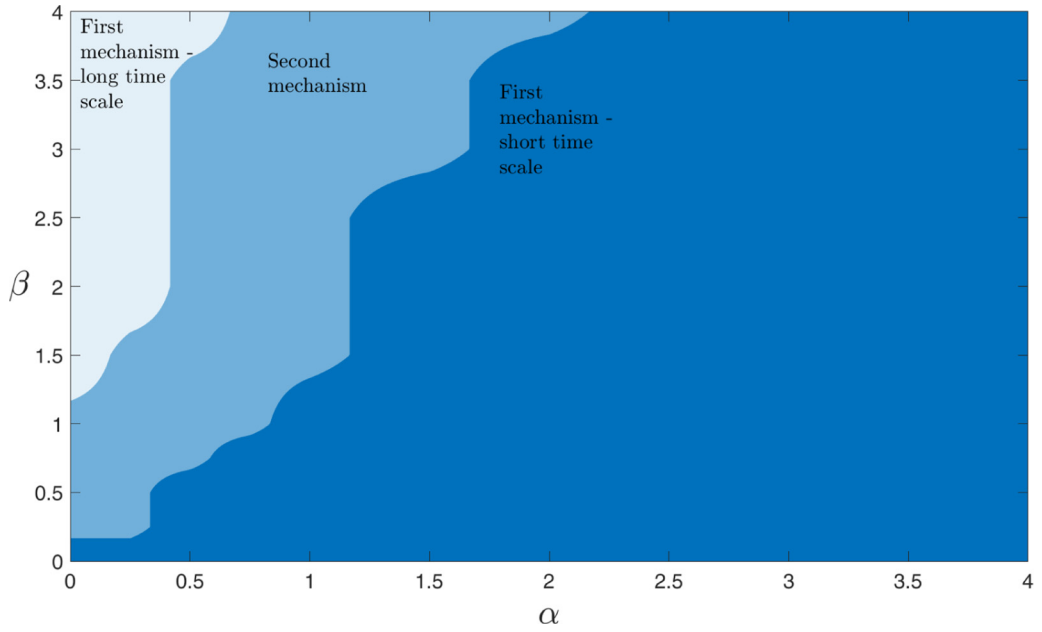

FIG. 26. Values of the spatial wavenumbers for which the optimal energy gain mechanism changes for $\mathrm{Ri}_\tau = 120$. This map is obtained by assigning each combination of α and β a value denoting the dominant mechanism: 10 for the first (short timescale), 0 for the second, and -10 to the first (long timescale).

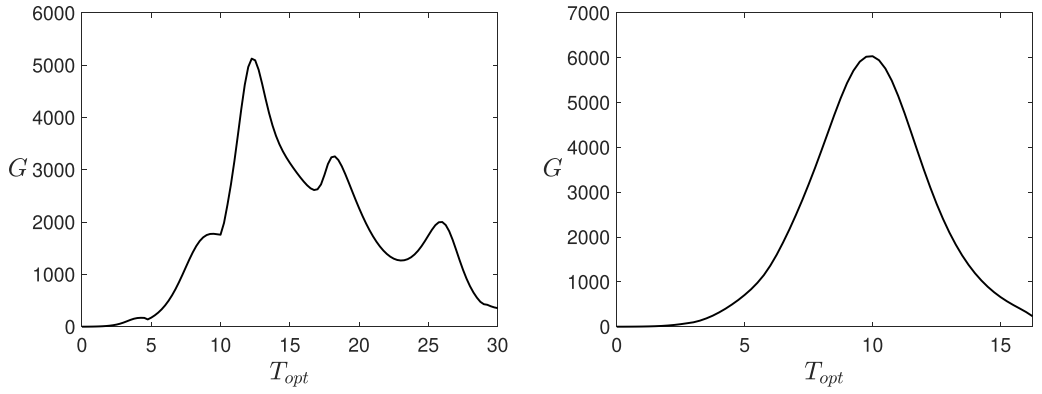

FIG. 27. Optimal energy gain versus T_{opt} for $\text{Ri}_\tau = 480$, $\alpha = 0$, and $\beta = 2.2$ (left), $\beta = 6$ (right).

$\alpha = 0$, this can be observed in Fig. 27, showing the energy gain curves for two values of β in the range $\in [1, 6]$, for which a strong energy growth is found (see left frame of Fig. 7). The shape of the energy curve for $\beta = 2.2$ closely resembles that observed in the optimal case at $\text{Ri}_\tau = 120$, showing the presence of three distinct peaks, followed by further energy oscillations due to the beating phenomenon. However, for larger values of β, only one peak is recovered, at rather slow time, as shown in the right frame of Fig. 27. Despite these differences in the energy gain curves, for $\alpha = 0$ the optimal mechanism leading to these large-scale energy gain peaks appears to be similar to the previous cases, i.e., a generalization of the lift-up mechanism. However, for larger values of β we observe an increasing asymmetry in the optimal perturbations, clearly shown by the optimal profiles in the right frame of Fig. 28, probably due to the shielding effect of the core of the channel,

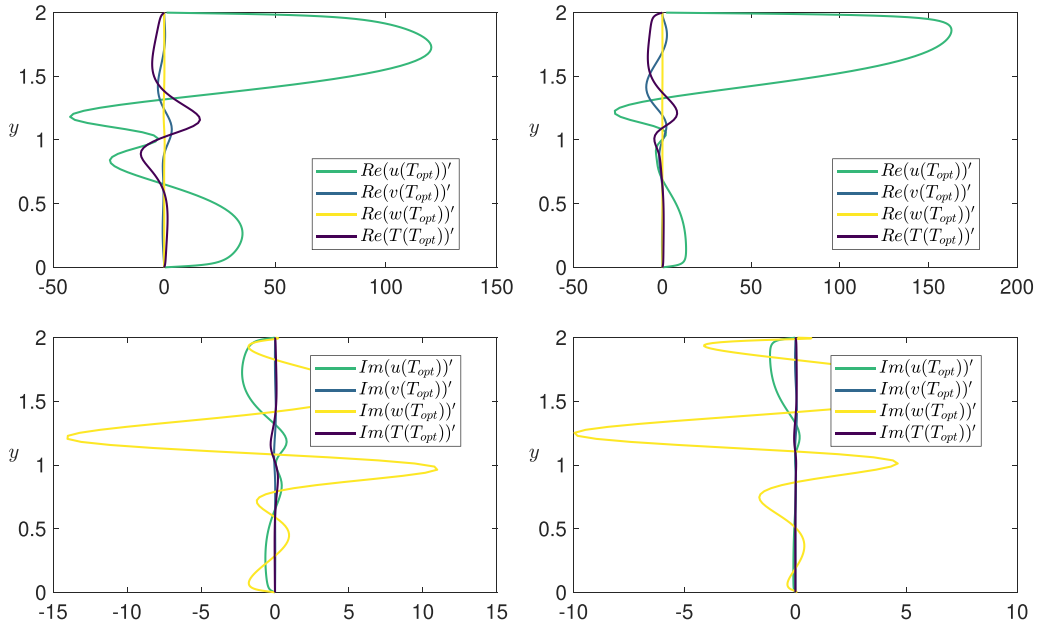

FIG. 28. Real part (upper frames) and imaginary part (lower frames) of the optimal perturbation at $\text{Ri}_\tau = 480$ for $(\alpha, \beta) = (0, 2.2)$ and $T_{\text{opt}} = 12.3$ (left), $(\alpha, \beta) = (0, 6)$ and $T_{\text{opt}} = 9.9$ (right).

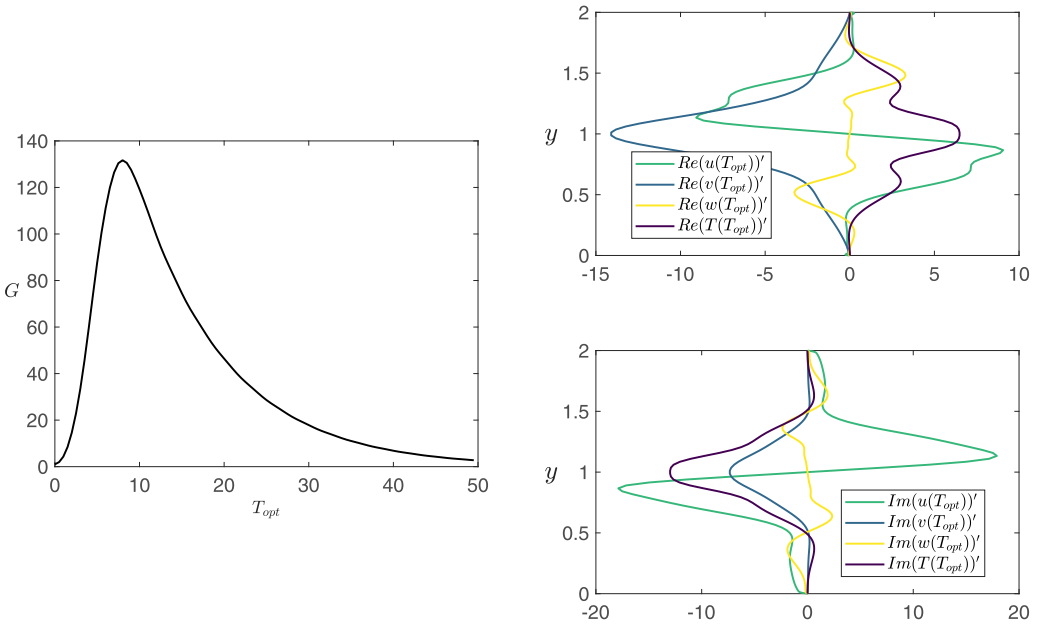

FIG. 29. Optimal energy gain versus T_{opt} for $\text{Ri}_\tau = 480$, $\alpha = 2.5$, and $\beta = 0.5$ (left) and real (top right) and imaginary (bottom right) part of the optimal perturbation at $\text{Ri}_\tau = 480$ for $(\alpha, \beta) = (2.5, 0.5)$.

as observed in the DNS. This behavior is linked to the increase of the effect of buoyancy over convection, as the temperature field is asymmetrical, unlike the velocity one.

2. Streamwise-dependent perturbations ($\alpha \neq 0$)

For strong stratification, as shown in Fig. 6, the contours of G_{max} considerably extend towards higher values of α, leading to energy amplification of three orders of magnitude for values of α up to 2. For increasing values of $\alpha > \beta$, the main amplification mechanism is that generating a central temperature streak at optimal time, shown in Fig. 29 for a case with $\alpha = 2.5$ and $\beta = 0.5$. The two-dimensional view in Fig. 30 shows the alternating temperature patches created at target time at the center of the channel, corresponding with small vortices in the x-y plane. Coherent flow structures

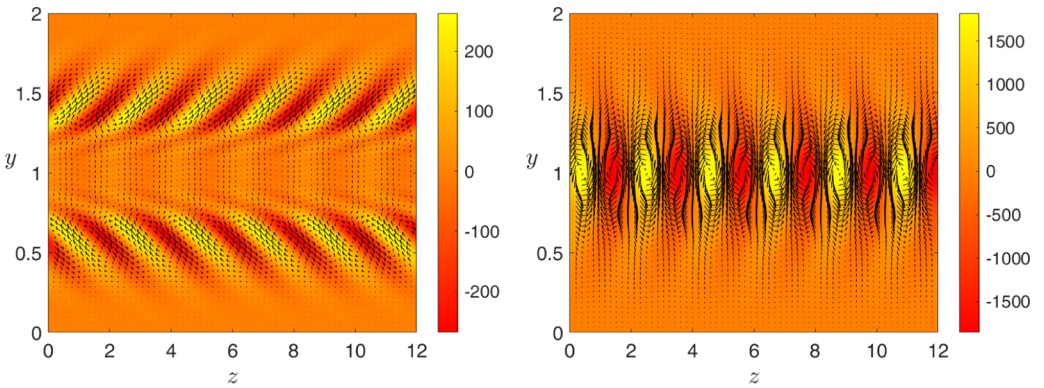

FIG. 30. Optimal perturbation at time $t = 0$ (left) and $t = T_{\text{opt}}$ (right) for $\alpha = 2.5$, $\beta = 0.5$, and $\text{Ri}_\tau = 480$ in the plane x-y. Shaded contours of temperature and vectors of $u' - v'$.

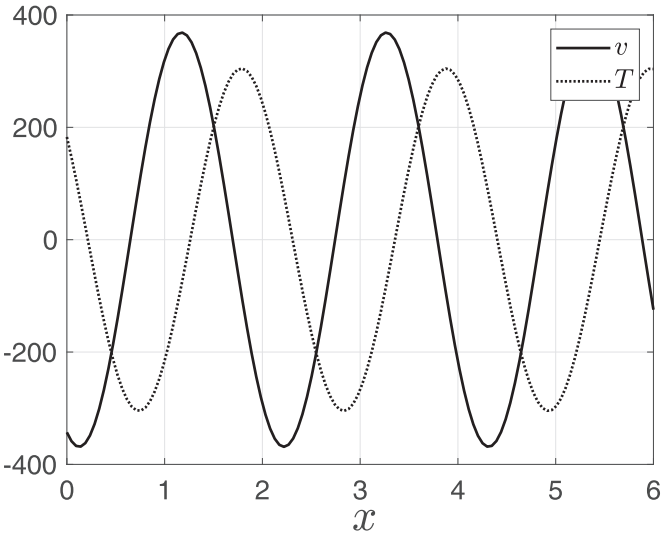

FIG. 31. Temperature T' and wall-normal velocity v' perturbations for the optimal disturbance at $\mathrm{Ri}_\tau = 480$, $\alpha = 2.5$, and $\beta = 0.5$.

with short streamwise and long spanwise wavelength placed towards the center of the channel are typically observed in numerical simulations of the same flow case [21,42] and linked to internal gravity waves. It is known that in the linear gravity waves, the phase difference between vertical motions and temperature will be $\pm\pi/2$ [1,43]. Figure 31 clearly shows that the optimal v' and T' perturbations inducing a central temperature peak at the center of the channel are characterized by a phase lag of $\pi/2$ rad, being thus consistent with the development of internal gravity waves reported in the DNS [21].

IV. CONCLUSIONS

In turbulent flows, the energy-containing coherent structures populating the flow are often linked to unstable or optimally growing perturbations of the mean flow. A notable example are the wall- and large-scale streaks in a turbulent channel [44] and the rolls in unstable stratified channel flows [19]. In order to get insights on the origin of coherent structures in the less investigated case of the stably stratified turbulent channel flow, in this work modal and nonmodal stability of the mean turbulent flow has been performed for three different values of the friction Richardson number, namely, $\mathrm{Ri}_\tau = 60$, 120, and 480. The aim is to assess the influence of stable stratification on the main features of the most unstable and/or optimally growing structures.

Modal stability analysis has shown that the eigenvalue spectrum is influenced by the value of Ri_τ, although for the values of Ri_τ considered, the flow remains always asymptotically stable. Notably, for sufficiently high Ri_τ, an interaction between stable modes having similar growth rate has been found to induce a low-frequency beating phenomenon. Concerning the nonmodal stability analysis, we have observed that the optimally growing structures are found for zero streamwise wavenumber, as in the unstratified turbulent case, but differently from the stratified laminar case. However, an increase of the friction Richardson number, Ri_τ, at fixed friction Reynolds number, Re_τ, translates into a magnification of the energy gain at the outer peak of two orders of magnitude. At the same time, the spanwise wavenumber for which the energy gain peaks has been found to increase with Ri_τ, reaching up to four times its value for the unstratified case. For the highest Ri_τ considered, the values of β for which a very high energy gain is observed are comparable to those corresponding to the "outer" regions of high spectral densities reported in the DNS of stably

stratified turbulent channels [21], namely, $\beta \in [1, 6]$. The present results thus suggest that the strong alterations observed in the energy-carrying large-scale coherent structures at high Ri_τ may be due to changes in the transient energy-growth mechanisms induced by the presence of a stable thermal stratification.

At the same time, the peak value of the optimal gain for the inner peak slightly increases at moderate Ri_τ. However, an inner peak is no longer observed for $\mathrm{Ri}_\tau = 480$. For this value of Ri_τ, the range of spanwise wavenumbers allowing a strong energy growth is very large, leading to the presence of different peaks for low values of β, but totally hiding the energy gain peak associated to the inner-scale dynamics. This corroborates the observation made through DNS [21], that the coherent structures at the wall are not altered by the presence of stable stratification.

For nonzero values of the streamwise, α, and spanwise, β, wavenumbers, the energy gain curve shows two or even three different peaks, related to different mechanisms. The optimum occurring at shorter target times leads at the optimal time to a center-channel temperature peak, whereas a modified lift-up mechanism is observed at slightly larger target times. In general, it has been found that for $\alpha < \beta$ the lift-up mechanism prevails whereas for $\beta > \alpha$ the centerline-temperature mechanism dominates the growth. In the former case the strongest term in the perturbation energy budget is that of velocity production, followed by that of temperature production, while the other terms are negative almost during the whole time evolution. This confirms that in this case the amplification mechanism may be linked to a velocity-based mechanism such as the lift-up mechanism, which created high-amplitude velocity and temperature streaky structures. However, for larger values of α, the strongest energy-budget term is that of temperature production, followed by that of velocity production, indicating that this mechanism is mostly driven by the increase of the potential energy rather than the kinetic one, and it is intimately linked to the presence of stratification. Increasing the Ri_τ to the largest considered value, we observe an increasing asymmetry in the optimal perturbations for larger values of β, which is similar to the behavior observed in the DNS by Garcia-Villalba and Del Alamo [21], which has been ascribed by these authors to the shielding effect of the core of the channel. This behavior is linked to the increase of the effect of buoyancy over convection, as observed in previous DNS [21]. Moreover, for the stronger stratification considered here, a large amplification is found also for optimal perturbations with streamwise wavenumber much larger than the spanwise one. This perturbation inducing temperature patches at the center channel phase lagged of $\pi/2$ with the wall-normal velocity, similarly to gravity waves recovered in the DNS for sufficiently large stratification.

The present work has thus identified several optimally growing structures having features resembling those of previous DNS observations. However, a one-to-one comparison of the rms velocity profiles, wavenumber spectra, and other flow statistics has not been possible, due to the very limited availability of literature data on stably stratified turbulent channel flows. Future works will aim at carrying out DNSs of the considered flow cases to be directly compared to the stability results discussed here. The availability of these new DNS data would provide us an opportunity to extend the analysis to higher Reynolds and Richardson numbers. Moreover, we will aim at extending the present analysis to different flow cases, such as the turbulent stably stratified atmospheric boundary layer flow, whose coherent structures are highly relevant for the field of wind turbine flows.

APPENDIX A: TURBULENT UNSTRATIFIED CASE RESULTS

For the unstratified turbulent case, we used the same equations proposed in Sec. II, but the approach to eddy viscosity was different. In fact, for the range of Re_τ considered, the analytical relation of Cess [25] turns out to be an excellent solution, while for the mean velocity profile, the differential relation proposed by Reynolds and Tiederman was used [14]:

$$\nu_T^+(\eta) = \frac{1}{2}\left(1 + \frac{k^2\mathrm{Re}_\tau^2}{9}(1-\eta^2)^2(1+2\eta^2)^2[1-e^{(|\eta|-1)\mathrm{Re}_\tau/A}]^2\right)^{1/2} + \frac{1}{2}, \tag{A1}$$

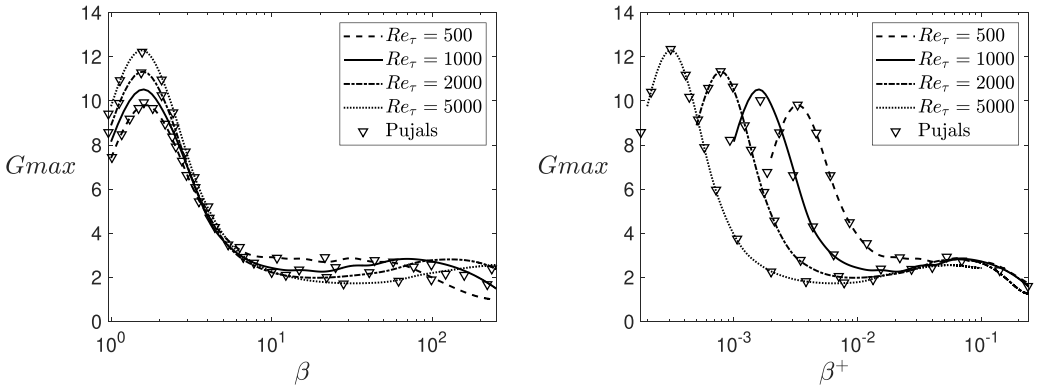

FIG. 32. $G_{\max}$ versus β with $\alpha = 0$ for different values of Re_τ in outer scale (left) and inner scale (right).

$$\frac{dU^+}{d\eta} = \frac{\mathrm{Re}_\tau \eta}{\nu_T^+(\eta)}, \tag{A2}$$

where $\mathrm{Re}_\tau = u_\tau h/\nu$, $U^+ = U/u_\tau$, $\eta = y/h$, $\nu_\tau^+ = \nu_T/\nu$, and k and A are two constants $A = 25.4$, $k = 0.426$.

Following what has been done by Pujals *et al.*, we started by considering uniform structures in the streamwise direction, i.e., we fixed $\alpha = 0$, but while they worked on the inner scale starting from the turbulent Orr-Sommerfeld-Squire equations we worked on the primitive formulation. We considered four cases, namely, $\mathrm{Re}_\tau = 500$, 1000, 2000, and 5000. In Fig. 32 it is possible to observe how the outer and inner peaks coincide for the different Re_τ considered. The outer peak corresponds to a wavelength $\lambda_z \approx 4$ which is the same found by Pujals *et al.* but is different from the one found by Del Alamo and Jiménez [26]; moreover the value of the $G_{\max}$ slightly increases with Re_τ.

APPENDIX B: WALL-NORMAL ENERGY FLUX

We start by considering Eq. (6b) written in Cartesian tensor notation:

$$\frac{\partial u_i'}{\partial t} = -u_j' \frac{\partial \overline{u}_i}{\partial x_j} - \overline{u}_j \frac{\partial u_i'}{\partial x_j} - \frac{\partial p}{\partial x_i} + \frac{1}{\mathrm{Re}}\left[\frac{\partial \overline{\nu}_t}{\partial x_j}\left(\frac{\partial u_i'}{\partial x_j} + \frac{\partial u_j'}{\partial x_i}\right) + \overline{\nu}_T \frac{\partial^2 u_i'}{\partial x_j^2}\right] - \mathrm{Ri} T' \mathbf{e}_i. \tag{B1}$$

By performing the scalar product with u_i' we get

$$\frac{\partial \frac{1}{2} u_i' u_i'}{\partial t} = \underbrace{-u_i' u_j' \frac{\partial \overline{u}_i}{\partial x_j}}_{I} - \overline{u}_j \frac{\partial \frac{1}{2} u_i' u_i'}{\partial x_j} \underbrace{- u_i' \frac{\partial p}{\partial x_i}}_{II} + \frac{1}{\mathrm{Re}}\left[\frac{\partial \overline{\nu}_t}{\partial x_j}\frac{\partial \frac{1}{2} u_i' u_i'}{\partial x_j} + u_i' \frac{\partial \overline{\nu}_t}{\partial x_j}\frac{\partial u_j'}{\partial x_i} + \underbrace{u_i' \overline{\nu}_T \frac{\partial^2 u_i'}{\partial x_j^2}}_{III}\right], \tag{B2}$$

where

$$II = \frac{\partial (u_i' p)}{\partial x_i} - p\frac{\partial u_i'}{\partial x_i} = \frac{\partial}{\partial x_j}(p u_i' \delta_{ij}),$$

$$III = \frac{1}{\mathrm{Re}}\overline{\nu}_T \frac{\partial}{\partial x_j}\left(u_i' \frac{\partial u_i'}{\partial x_j}\right) - \frac{1}{\mathrm{Re}}\overline{\nu}_T \frac{\partial u_i'}{\partial x_j}\frac{\partial u_i'}{\partial x_j} = \frac{1}{\mathrm{Re}}\overline{\nu}_T \frac{\partial^2}{\partial x_j^2}\left(\frac{1}{2} u_i' u_i'\right) - \frac{1}{\mathrm{Re}}\overline{\nu}_T \left(\frac{\partial u_i'}{\partial x_j}\right)^2.$$

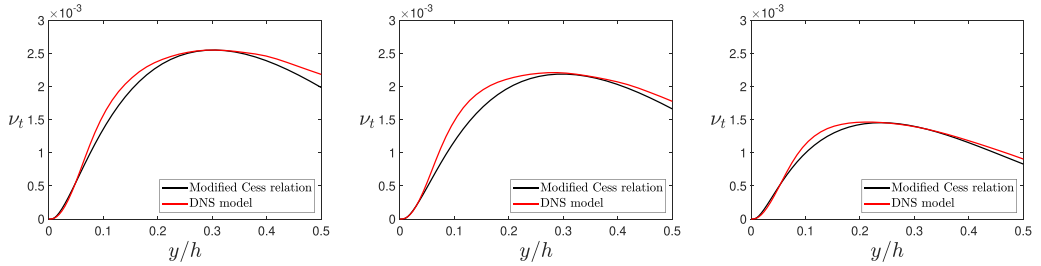

FIG. 33. Comparison for ν_t at $\mathrm{Ri}_\tau = 60$ (left), $\mathrm{Ri}_\tau = 120$ (middle), and $\mathrm{Ri}_\tau = 480$ (right).

We can replace these three terms and rearrange Eq. (B2) as follows:

$$\left(\frac{\partial}{\partial t} + \overline{u}_j \frac{\partial}{\partial x_j} - \frac{1}{\mathrm{Re}} \overline{\nu}_T \frac{\partial^2}{\partial x_j^2}\right) \frac{u_i' u_i'}{2} + \frac{\partial}{\partial x_j}(u_i' p)$$
$$= -u_i' u_j' \frac{\partial \overline{u}_i}{\partial x_j} - \frac{1}{\mathrm{Re}} \overline{\nu}_T \left(\frac{\partial u_i'}{\partial x_j}\right)^2 + \frac{\partial \overline{\nu}_t}{\partial x_j} \frac{\partial \frac{1}{2} u_i' u_i'}{\partial x_j} + u_i' \frac{\partial \overline{\nu}_t}{\partial x_j} \frac{\partial u_j'}{\partial x_i}. \tag{B3}$$

The equation is similar to that presented by Farano *et al.* [40] with the difference that here the nonlinear terms are missing, but in addition we have the turbulent terms described by eddy viscosity. When Eq. (B3) is integrated in the x direction and z direction, it describes the wall-normal transport of energy and the flux in the y direction can be simply identified as $\phi = p'v'$.

APPENDIX C: VALIDATION OF THE MODIFIED CESS MODEL

Due to the oscillations present in the profiles of the eddy viscosity ν_t and the eddy diffusivity κ_t we have used the modified Cess formulation as done by Vico [28] after adjusting some parameters to have a better overlap with DNS.

Figures 33 and 34 provide a comparison between the curves obtained directly with the relations (5) and those obtained with the analytical formulation in Eqs. (7)–(10). The comparison has been made in the area close to the wall, $y/h < 0.5$, where the oscillations are lower for the DNS model.

A good agreement can be observed for the two profiles, thus justifying the use of this analytical formulation.

APPENDIX D: SINGULAR VALUE DECOMPOSITION FOR THE OPTIMAL CASE AT $\mathrm{Ri}_\tau = 120$

In Sec. III B we have shown that in the optimal case at $\mathrm{Ri}_\tau = 120$, $\alpha = 0$, and $\beta = 2.597$ the gain curve has three distinct peaks. One might think at first that the three peaks are related to three

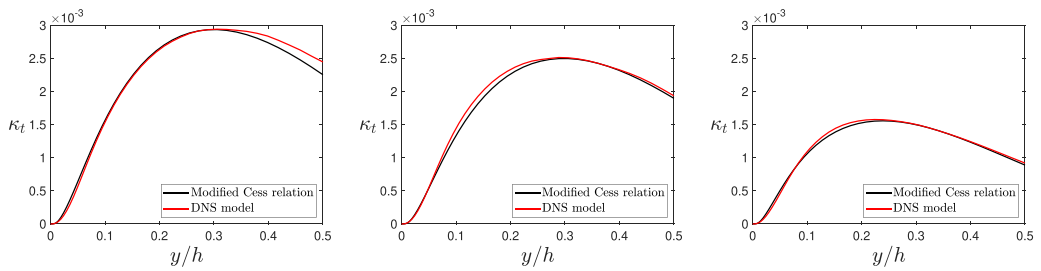

FIG. 34. Comparison for κ_t at $\mathrm{Ri}_\tau = 60$ (left), $\mathrm{Ri}_\tau = 120$ (middle), and $\mathrm{Ri}_\tau = 480$ (right).

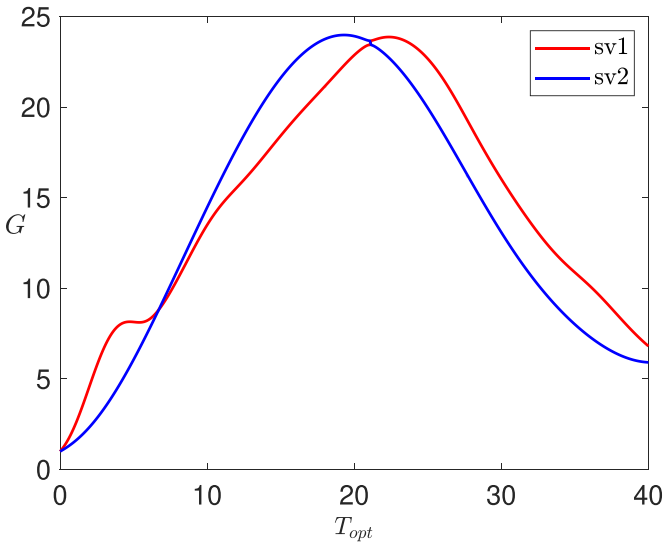

FIG. 35. Singular value decomposition for the case at $\mathrm{Ri}_\tau = 120$, $\alpha = 0$, and $\beta = 2.597$ with a constant prefactor for the potential energy.

different mechanisms by observing the behavior of the optimal perturbations, but only an SVD analysis can actually prove this.

We thus performed the optimization using the SVD, despite that for the potential energy a constant prefactor (1 in our case) must be used to avoid the optimization of a seminorm. Despite the use of a different prefactor than in the direct-adjoint method, it can be seen in Fig. 35 that the shape of the gain curve is quite similar and that the three peaks present are due to the switching of only two singular values.

[1] J. S. Turner and J. S. Turner, *Buoyancy Effects in Fluids* (Cambridge University Press, Cambridge, UK, 1979).
[2] S. A. Thorpe, *The Turbulent Ocean* (Cambridge University Press, Cambridge, UK, 2005).
[3] R. A. Brown, Longitudinal instabilities and secondary flows in the planetary boundary layer: A review, Rev. Geophys. **18**, 683 (1980).
[4] D. Etling and R. A. Brown, Roll vortices in the planetary boundary layer: A review, Boundary-Layer Meteorol. **65**, 215 (1993).
[5] K. S. Gage and W. H. Reid, The stability of thermally stratified plane poiseuille flow, J. Fluid Mech. **33**, 21 (1968).
[6] T. Asai, Stability of a plane parallel flow with variable vertical shear and unstable stratification, J. Meteorol. Soc. Jpn. **48**, 129 (1970).
[7] J. John Soundar Jerome, J.-M. Chomaz, and P. Huerre, Transient growth in Rayleigh-Bénard-Poiseuille/Couette convection, Phys. Fluids **24**, 044103 (2012).
[8] D. Biau and A. Bottaro, The effect of stable thermal stratification on shear flow stability, Phys. Fluids **16**, 4742 (2004).
[9] G. Facchini, B. Favier, P. Le Gal, M. Wang, and M. Le Bars, The linear instability of the stratified plane Couette flow, J. Fluid Mech. **853**, 205 (2018).
[10] E. Parente, J. C. Robinet, P. De Palma, and S. Cherubini, Modal and nonmodal stability of a stably stratified boundary layer flow, Phys. Rev. Fluids **5**, 113901 (2020).

[11] P. J. Schmid, D. S. Henningson, and D. F. Jankowski, Stability and transition in shear flows. Applied Mathematical Sciences, Vol. 142, Appl. Mech. Rev. **55**, B57 (2002).
[12] W. V. R. Malkus, Outline of a theory of turbulent shear flow, J. Fluid Mech. **1**, 521 (1956).
[13] B. J. McKeon and A. S. Sharma, A critical-layer framework for turbulent pipe flow, J. Fluid Mech. **658**, 336 (2010).
[14] W. C. Reynolds and W. G. Tiederman, Stability of turbulent channel flow, with application to Malkus's theory, J. Fluid Mech. **27**, 253 (1967).
[15] W. C. Reynolds and A. K. M. F. Hussain, The mechanics of an organized wave in turbulent shear flow. Part 3. Theoretical models and comparisons with experiments, J. Fluid Mech. **54**, 263 (1972).
[16] G. Pujals, M. García-Villalba, C. Cossu, and S. Depardon, A note on optimal transient growth in turbulent channel flows, Phys. Fluids **21**, 015109 (2009).
[17] A. Madhusudanan, S. J. Illingworth, I. Marusic, and D. Chung, Navier-Stokes–based linear model for unstably stratified turbulent channel flows, Phys. Rev. Fluids **7**, 044601 (2022).
[18] S. Pirozzoli, M. Bernardini, R. Verzicco, and P. Orlandi, Mixed convection in turbulent channels with unstable stratification, J. Fluid Mech. **821**, 482 (2017).
[19] C. Cossu, Onset of large-scale convection in wall-bounded turbulent shear flows, J. Fluid Mech. **945**, A33 (2022).
[20] M. A. Ahmed, H. J. Bae, A. F. Thompson, and B. J. McKeon, Resolvent analysis of stratification effects on wall-bounded shear flows, Phys. Rev. Fluids **6**, 084804 (2021).
[21] M. García-Villalba and J. C. Del Alamo, Turbulence modification by stable stratification in channel flow, Phys. Fluids **23**, 045104 (2011).
[22] P. Luchini, Reynolds-number-independent instability of the boundary layer over a flat surface: Optimal perturbations, J. Fluid Mech. **404**, 289 (2000).
[23] E. Parente, Modal and non-modal stability analysis in stratified shear flows, Master's report, DynFluid Laboratory, ENSAM, Paris, 2018.
[24] D. Koppel, On the stability of flow of a thermally stratified fluid under the action of gravity, J. Math. Phys. **5**, 963 (1964).
[25] R. D. Cess, A survey of the literature on heat transfer in turbulent tube flow, Research Report No. 8-0529-R24, Westinghouse, 1958.
[26] J. C. del Álamo and J. Jiménez, Linear energy amplification in turbulent channels, J. Fluid Mech. **559**, 205 (2006).
[27] C. Cossu, G. Pujals, and S. Depardon, Optimal transient growth and very large-scale structures in turbulent boundary layers, J. Fluid Mech. **619**, 79 (2009).
[28] C. Y. Vico, Transient development of perturbation in a stratified turbulent shear flow, Master's thesis, Institute of Thermal Turbomachinery, University of Karlsruhe (TH), 2008.
[29] H. Schlichting, *Boundary Layer Theory* (Springer-Verlag, Berlin, 1979).
[30] A. Michalke, On spatially growing disturbances in an inviscid shear layer, J. Fluid Mech. **23**, 521 (1965).
[31] L. N. Trefethen, *Spectral Methods in MATLAB* (SIAM, Philadelphia, 2000).
[32] D. P. G. Foures, C. P. Caulfield, and P. J. Schmid, Variational framework for flow optimization using seminorm constraints, Phys. Rev. E **86**, 026306 (2012).
[33] R. S. Blumenthal, A. K. Tangirala, R. I. Sujith, and W. Polifke, A systems perspective on non-normality in low-order thermoacoustic models: Full norms, semi-norms and transient growth, Int. J. Spray Combust. Dyn. **9**, 19 (2017).
[34] P. Luchini and A. Bottaro, An introduction to adjoint problems, Annu. Rev. Fluid Mech. **46**, 493 (2014).
[35] M. Farano, S. Cherubini, J.-C. Robinet, and P. De Palma, Subcritical transition scenarios via linear and nonlinear localized optimal perturbations in plane poiseuille flow, Fluid Dyn. Res. **48**, 061409 (2016).
[36] D. P. G. Foures, C. P. Caulfield, and P. J. Schmid, Localization of flow structures using infinity-norm optimization, J. Fluid Mech. **729**, 672 (2013).
[37] M. T. Landahl, A note on an algebraic instability of inviscid parallel shear flows, J. Fluid Mech. **98**, 243 (1980).
[38] S. C. Reddy and D. S. Henningson, Energy growth in viscous channel flows, J. Fluid Mech. **252**, 209 (1993).

[39] W. M. F. Orr, The stability or instability of the steady motions of a perfect liquid and of a viscous liquid. Part I: A perfect liquid. Part II: A viscous liquid, Proc. R. Irish. Acad. **27**, 69 (1907).

[40] M. Farano, S. Cherubini, J.-C. Robinet, and P. De Palma, Optimal bursts in turbulent channel flow, J. Fluid Mech. **817**, 35 (2017).

[41] J. Jiménez, The physics of wall turbulence, Physica A **263**, 252 (1999).

[42] O. Iida, N. Kasagi, and Y. Nagano, Direct numerical simulation of turbulent channel flow under stable density stratification, Int. J. Heat Mass Transf. **45**, 1693 (2002).

[43] R. B. Stull, *An Introduction to Boundary Layer Meteorology* (Springer Science & Business Media, 1988), Vol. 13.

[44] C. Cossu and Y. Hwang, Self-sustaining processes at all scales in wall-bounded turbulent shear flows, Philos. Trans. R. Soc. London A **375**, 20160088 (2017).